Materials Advances

ROYAL SOCIETY OF CHEMISTRY

REVIEW

View Article Online
View Journal | View Issue

Cite this: *Mater. Adv.*, 2025, **6**, 9340

A review of rare earth ruthenate pyrochlores as OER electrocatalysts in acidic media

Megan Heath, * Svein Sunde and Frode Seland

Ruthenate pyrochlores are highly tunable structures and promising OER electrocatalysts in both acidic and alkaline media. These structures provide a platform to balance activity, stability, and cost. This review critically examines the structural, electronic, and catalytic properties of rare-earth ruthenate pyrochlores, with a focus on how A- and B-site modifications and doping influence OER performance. We highlight the role of mixed-valence states, B–O covalency, and lattice distortions in enhancing catalytic activity, while also addressing the challenges of catalyst degradation and dissolution. Design strategies to further improve activity and stability are not clearly outlined in the literature, although the majority of studies incorporate acceptor doping to induce oxygen vacancies or mixed B-site valence. Furthermore, the review underscores the need for standardised electrochemical testing protocols. By consolidating recent advances and identifying structure–property relationships, this work provides a guideline for the rational design of pyrochlore OER electrocatalysts, as well as recommendations for how stability and activity should be evaluated.

Received 30th June 2025,
Accepted 29th September 2025

DOI: 10.1039/d5ma00696a

rsc.li/materials-advances

1 Introduction

Finding a suitable electrocatalyst for the oxygen evolution reaction (OER), especially in acidic media, remains one of the main challenges for the large-scale implementation of water electrolysis. This is particularly true for proton exchange membrane (PEM) water electrolysis (PEMWE), where the highly oxidising and acidic environment demands robust anode materials. PEMWE is a promising technology, offering flexible electrolyser design, high-purity hydrogen, compatibility with fluctuating renewable energy sources, and rapid start-up and shut-down. Thus, the development of a viable anodic PEM electrocatalyst is essential. A schematic representation of a PEM water electrolysis cell can be seen in Fig. 1.

Currently, the state-of-the-art OER electrocatalyst is IrO_2. However, the extreme scarcity and high cost of iridium undermine its long-term practicality. Ruthenium and its oxides exhibit even greater OER activity, yet they suffer from poor stability under OER conditions. Stabilising ruthenium would be ideal, as it is the most affordable and more abundant platinum-group metal.[1] One common strategy is to create mixed Ru–Ir oxides, although none have exceeded the activity of Ru or the stability of Ir.[2,3] Other mixed oxides, such as perovskites, have been explored, but often lack stability under acidic OER conditions. Pyrochlores have been investigated for OER applications since the early 1980s,[4] and has gained renewed interest in recent years due to its high tunability, enabling optimisation of both activity and stability.

Although several reviews on pyrochlores for OER applications have been published,[5–7] this review specifically highlights the potential of ruthenate pyrochlores as OER electrocatalysts in acidic environments. It is intended as a practical guide for both new and experienced researchers. Significant findings have emerged since the most recent review, and new conclusions may be drawn from their aggregation. We begin by detailing the structure of pyrochlores, followed by an overview of the OER process and an exploration of pyrochlores as promising electrocatalysts. Based on the knowledge presented, we offer suggestions for future compositions and strategies tailored to OER applications. We also provide guidelines for

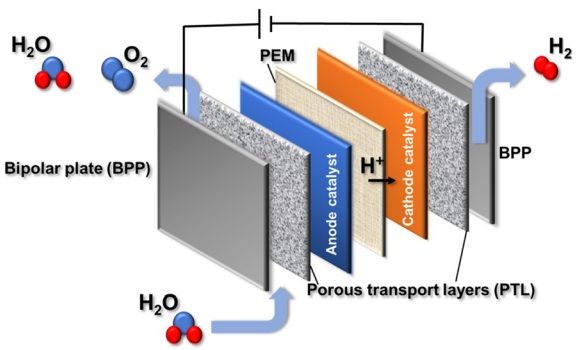

Fig. 1 Illustration of a single cell used in PEM water electrolysis.

The Norwegian University of Science and Technology, Department of Materials Science and Engineering, N-7491, Trondheim, Norway.
E-mail: megan.heath@ntnu.no

examining the electrocatalytic activity and stability of these materials.

Pyrochlores are technologically relevant ternary metallic oxides with the general formula $A_2B_2O_7$. They are sometimes expressed as $A_2B_2O_{7-\delta}$ to reflect intrinsic oxygen vacancies, or as $A_2B_2O_6O'$ since O and O′ occupy distinct crystallographic sites. Structurally, the pyrochlore can be derived from the fluorite lattice by removing one out of eight anions in a partially ordered manner, resulting in a halved unit cell parameter.[8–10]

The pyrochlore structure is named after the mineral pyrochlore, $(Na,Ca)_2Nb_2O_6(F,OH)$, which forms reddish-brown octahedral crystals, first discovered in 1826 in Larvik, Norway by F. Wöhler.[11] These compounds are widely occurring, as nearly every element on the periodic table can be incorporated at different sites within the structure. This high degree of tunability accounts for their wide range of physical properties, spanning semiconducting to metallic, ferromagnetic, ferrimagnetic, ferroelectric, piezoelectric, luminescent, and ionically conductive behaviours.[12,13] Due to this versatility, pyrochlores find use in numerous applications including nuclear waste immobilization, giant magnetoresistors, sensors, luminescence materials, (electro)catalysts, catalyst supports, solid electrolytes, thermal barrier coatings, and air-fired thick film resistors.[8,10,13–15] Recently, pyrochlores have attracted growing interest as anode electrocatalyst materials for proton exchange membrane (PEM) electrolysers, owing to their ability to stabilise the active Ru site within the structure.[6]

1.1 Crystal structure and symmetry

The pyrochlore structure belongs to the space group $Fd\bar{3}m$ (227), corresponding to a face-centered cubic Bravais lattice with point group $m\bar{3}m$. It features a glide plane (d) parallel to the a-axis, a threefold inversion axis along [111], and a mirror plane in [110]. Both A- and B-site cations occupy inversion centers.[16] As a cubic system, pyrochlores have a single lattice parameter a, typically between 9.5 and 11.5 Å.[10]

Each unit cell contains eight $A_2B_2O_6O'$ formula units (Z = 8),[15] totaling 88 atoms and illustrating the structural complexity.[10] The unit cell (Fig. 2) includes four nonequivalent atom types occupying five distinct sites. Taking the B-site cation as the origin, the A- and B-sites (both with $\bar{3}m$, D_{3d} symmetry) occupy Wyckoff positions 16d $\left(\frac{1}{2},\frac{1}{2},\frac{1}{2}\right)$ and 16c (0, 0, 0), respectively.[14,17] Their multiplicities (16) follow from the eight molecules per unit cell and the stoichiometry (which is 2 for both the A- and B site).

The O and O′ atoms occupy 48f $\left(x,\frac{1}{8},\frac{1}{8}\right)$ with mm (C_{2v}), and 8b $\left(\frac{3}{8},\frac{3}{8},\frac{3}{8}\right)$ with $\bar{4}3m$ (T_d) symmetry, respectively.[17] The variable positional parameter x determines the M–O bond lengths and hence the A- and B-site coordination environments.[17] The (111) XRD peak is particularly sensitive to the 48f position, and the refined x-value indicates if the pyrochlore is ideal, or a defect fluorite.[18] The fifth crystallographic site, 8a $\left(\frac{1}{8},\frac{1}{8},\frac{1}{8}\right)$, is an unoccupied oxygen vacancy site (O″).[17]

All oxygen atoms are coordinated tetrahedrally by cations.[19] O in 48f is surrounded by two A- and two B-site cations, O′ in 8b is coordinated by four A-site cations, and the vacant 8a site is surrounded by four B-site cations (Fig. 3). While 8a and 8b have 48f as their only second-nearest oxygen neighbours, the 48f sites have all three oxygen sites as second-nearest neighbours, forming diffusion chains for vacancy-mediated oxygen transport.[19]

The A-site is typically occupied by larger, less charged cations (*e.g.*, rare earths), while the B-site contains smaller, more highly charged transition metals. The A- and B-site coordination environments are illustrated in Fig. 4. Pyrochlores can be classified based on cation valence combinations: (2+, 5+) or (3+, 4+).[17] Ruthenate pyrochlores can adopt both combinations due to the multiple valence states that Ru can adopt. (3+, 4+) variants are most common due to the abundance of A-cations adopting 3+ valence states, and these structures have been shown to be highly active towards the OER.[20]

A-site cations are eight-fold coordinated in distorted cubes (axially compressed scalenohedra), with shorter A–O′ (8b, ~2.3 Å) and longer A–O (48f, ~2.5 Å) bonds. B-site cations are six-fold coordinated by equidistant 48f oxygen atoms forming a trigonal antiprism.[16,17] The B–O octahedra form a corner-sharing network, while A-site cations construct an interpenetrating anti-SiO_2 lattice.[21] This framework also accommodates defect pyrochlores such as $A_2B_2O_6$ and AB_2O_6.[16]

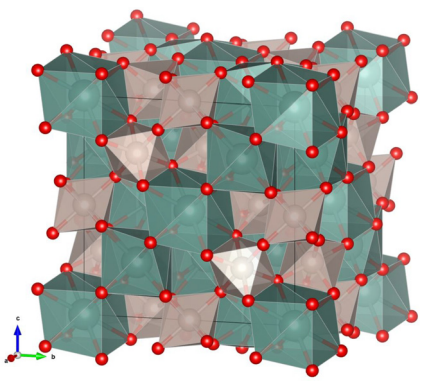

Fig. 2 The pyrochlore unit cell with the teal colour representing Y, the grey colour representing Ru and red representing oxygen.

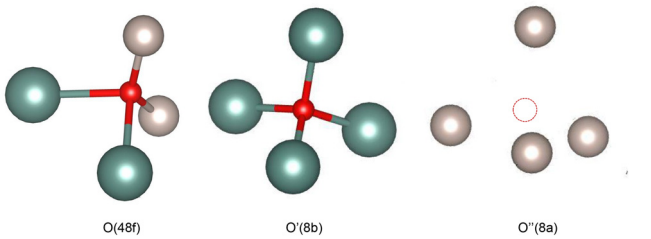

Fig. 3 Oxygen sites at 48f and 8b and the oxygen vacancy site at 8a in the pyrochlore unit cell. Red spheres represent oxygen; grey and teal represent Ru and Y, respectively.

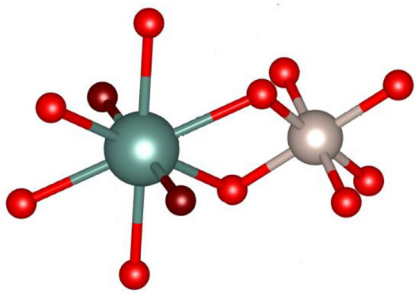

Fig. 4 A- and B-site metal coordination in the pyrochlore structure. Grey and teal spheres represent Ru and Y, respectively. Bright red spheres represent oxygen (O) in the 48f site, and dark red spheres oxygen (O′) in the 8b site.

Structurally, pyrochlores can be described as a network of corner-sharing BO_6 octahedra, with A and O′ occupying the resulting cage-like voids.[15] Notably, both A and O′ sites can be vacant without destabilizing the structure—facilitating cation and anion mobility.[15] In $A_2Ru_2O_6O'$, the RuO_6 octahedra link in a zigzag configuration, forming Ru–O–Ru angles of 135°.[21] Given a and x as the sole structural variables, cation–oxygen distances can be calculated as follows:[22]

$$d[\mathrm{B}-\mathrm{O}] = a\sqrt{(x-1/4)^2+\frac{1}{32}} \quad (1)$$

$$d[\mathrm{B}-\mathrm{O}''] = a\frac{\sqrt{3}}{8} \quad (2)$$

$$d[\mathrm{A}-\mathrm{O}] = a\sqrt{(x-1/2)^2+\frac{1}{32}} \quad (3)$$

$$d[\mathrm{A}-\mathrm{O}'] = a\frac{\sqrt{3}}{8} \quad (4)$$

1.2 Phase transitions

The 3+, 4+ pyrochlore accommodates solid solutions between BO_2 and A_2O_3.[23] Its stability depends on the cation radius ratio (r_A/r_B), with the ordered structure favoured between 1.46–1.78.[17] Below 1.46, it transitions to a disordered fluorite phase.[24] A- and B-site cations typically measure >1 Å and *ca.* 0.6 Å, respectively.[25]

Fuentes *et al.* support cation radius ratio as a stability predictor and caution against tolerance factors due to antisite defects in pyrochlores.[24] Minervini and Grimes suggest atomistic simulations for better predictions, considering oxygen sublattice relaxation.[23] Because the energy gap between pyrochlore and fluorite phases is small, especially near stability limits, disorder is common.[19] For instance, $RE_2Hf_2O_7$ can crystallize as either phase, depending on synthesis.[26] Order–disorder transitions may arise from cationic or anionic effects.[24]

The positional parameter x, influenced by cation sizes and origin choice, also governs stability. With B as origin, stable pyrochlores exhibit $0.3125 \leq x \leq 0.375$.[17,22] For $Y_2Ru_2O_7$, x = 0.333.[16] As $x \rightarrow 0.375$, the structure tends toward defect fluorite, with antisite cation disorder and Frenkel anion pairs.[22] When A is the origin, the stability range is reported as $0.404 \leq x \leq 0.432$.[27] Within this range, BO_6 polyhedra approach octahedral symmetry, a key factor in pyrochlore formation.[27]

1.3 Electronic structure of pyrochlores

The electronic structures of pyrochlores are not fully understood, ranging from insulating to semiconducting and metallic.[28] Lead- and bismuth ruthenate pyrochlores exhibit high electronic conductivity (10–1000 Ω^{-1} cm^{-1}),[14] whereas yttrium and some lanthanide variants are insulators, despite being isostructural and isoelectronic.[28] Band theory classifies solids as metals or insulators based on whether or not their electronic structures consist of partially filled bands. For example, $Pb_2Ru_2O_7$ is metallic since the t_{2g} sub-band is partially filled. However, $Y_2Ru_2O_7$ is known as an insulator due to the additional splitting of its t_{2g} bands so that it consists of one filled and one empty band.[28,29] Therefore, it is categorised as a Mott insulator, which will subsequently be discussed in more detail.

To understand metal–nonmetal transitions in pyrochlore structures, it is emphasised that the classic Bloch–Wilson band theory does not hold for all crystalline solids.[9] This is because band theory uses a single particle approximation and does not take into account electron–electron interactions. In this sense, band theory only holds when the bandwidth (W) is larger than the coulomb repulsion (U) and does not take into account electron correlations in systems with $U > W$.[30] For these systems, other models are needed.

The Mott–Hubbard band model illustrates that as atoms move closer together, the lower Hubbard band (ionisation energy) and the upper Hubbard band (electron affinity) both broaden until they overlap at the band limit. This results in a sudden transition from an insulator to a metal, known as the Mott transition. Materials with band-gaps that involve the split Hubbard states are termed Mott-insulators. There is also a limited composition regime where materials remain insulating in the region where the upper- and lower Hubbard bands cross due to Anderson localisation (derived from randomness) of electronic states.[21,31] One must also take note of the so-called charge-transfer insulators, characterised by a considerable oxygen-p character of the top-filled band instead of metal d character. For these kinds of materials the charge transfer energy (Δ) defines the band gap instead of U. Δ is the energy cost of transferring an O 2p electron to a metal d orbital.

Determining Mott transitions in pyrochlores is complex. Cox *et al.* identified a metal-to-semiconductor transition at y = 1.55 in $Bi_{2-y}Gd_yRu_2O_7$.[21] They found that Bi^{3+} has a smaller effective radius in the metallic state due to Bi 6s electron density being transferred into Ru 4d states.[21] They observed an increased density of states (DOS) near the Fermi level, E_F, with increasing Bi content *via* ultraviolet photoelectron spectroscopy (UPS), high-resolution electron energy loss spectroscopy (HREELS) and X-ray photoelectron spectroscopy (XPS), attributing the transition to both disorder (Anderson) and correlation

(Hubbard) effects.[21,32] Strong Bi–O′ covalent interactions (due to the Bi $6s^2$ lone pair) in bismuth ruthenate pyrochlores weakens the Bi–O interaction and enlarges the Ru–O–Ru bond angle, broadening the t_{2g} band and allowing a Mott–Hubbard mechanism of electron delocalization.[14] Hsu and Kasowski found that Bi and Pb 6s bands lie too deep to contribute to conduction.[33] Instead, Bi 6p bands that lie closer to E_F hybridize with Ru 4d states through framework O atoms. Although the Bi 6s band is 4 eV deeper than that of Pb, its 6p band lies 3 eV closer to E_F than Pb's, resulting in twice the DOS at E_F, while Y exhibits minimal DOS, aligning with its Mott insulating behaviour.[33] Furthermore, Kanno *et al.* found that the conductivity of $Bi_{2-x}Y_xRu_2O_7$ decreases as x increases, correlating with greater RuO_6 distortion and a reduced Ru–O–Ru bond angle (from 139° at $x = 0$ to 129° at $x = 2$).[34] The metal-to-semiconductor transition occurs between $x = 1.2$ and $x = 1.4$. In the metallic regime ($x \leq 1.2$), Bi electrons contribute to the Ru 4d state, shortening the Ru–O bond length. No such variation is observed in the insulating regime.[34] From these works it can be seen that the A-cation strongly influences the electronic properties of ruthenate pyrochlores, as Ru(IV) 4d electrons lie near the localized-itinerant boundary.[14,21] For electrocatalysis, assessing 4d electron delocalisation is vital. Taira *et al.* found that magnetic behaviour (magnetic ordering in systems with localized electrons) can be a diagnostic tool.[35] Ruthenium dioxide, with an undistorted rutile structure, has itinerant electrons and is metallic.[21]

In pyrochlores, the B-site is coordinated octahedrally (4), splitting d orbitals into higher e_g and lower t_{2g} energy states. However, Ru often adopts a trigonal antiprismatic (D_{3d}) rather than octahedral (O_h) symmetry,[17] splitting t_{2g} into a filled e_g' and empty a_{1g} band.[28] Structural differences impact the electronic structure: in $Y_2Ru_2O_7$, the t_{2g} and e_g bands are 1 eV apart, while in $Bi_2Ru_2O_7$, partial band overlap places E_F in a DOS minimum.[28] The t_{2g} bandwidth in $Y_2Ru_2O_7$ is also 25% narrower than in $Bi_2Ru_2O_7$,[28] though the role of these factors in its insulating behaviour remains uncertain.

Corner-sharing transition metal oxides can develop wide enough t_{2g} bands for itinerant transport *via* M–O–M orbital overlap.[21] Small M–O–M angles hinder this, as in $Gd_2Ru_2O_7$ and $Y_2Ru_2O_7$, where competition from acidic A-site cations restricts O 2p orbital availability. A Ru–O–Ru angle below 130° is linked with semiconducting character.[36] $ARuO_3$ perovskites feature a 180° angle and ruthenate pyrochlores around 135°.[21] $Y_2Ru_2O_7$ has an angle of 120°, and $Bi_2Ru_2O_7$ 133°.[28] Cava questions whether small differences (*e.g.*, 2° between metallic Bi and insulating Pr pyrochlores) fully explain the transition.[28]

Doping is a proven strategy to tune conductivity. For instance, $Bi_{1.5-x}Ce_xSb_{1.5}CuO_7$ shows increased conductivity with Ce content.[25] Similarly, Sr-doping in $Y_{2-y}Sr_yRu_2O_7$ increases the Ru–O–Ru bond angle, enhances orbital overlap, and broadens the bandwidth, reducing electron correlations and closing the Mott–Hubbard gap.[29] Electronic structure can also be tuned through structural modification. Liu *et al.* demonstrated that implanted MoO_x species induce intermolecular charge transfer from RuO_6, delocalizing Ru 4d electrons and enlarging the Ru–O–Ru bond angle—removing the band gap.[37]

2 The oxygen evolution reaction (OER)

2.1 Adsorption

The Sabatier principle, central to heterogeneous catalysis, states that a catalyst should bind reactants neither too strongly nor too weakly.[38] Parsons later demonstrated that hydrogen adsorption strength plotted against hydrogen evolution rates form a volcano relationship, placing Pt at the apex.[39] Although the OER and ORR are more complex, volcano trends are still observed.

A quanum-mechanical description of chemisorption of intermediates in catalysis is provided by the Newns–Anderson model[40] and the related the Hammer–Nørskov d-band model.[41] The Newns–Anderson model considers the interaction between adsorbate energy levels (η_a) and the adsorbent's DOS, defined by its energy center (η_d), bandwidth (W), and coupling strength (V).[41] When W increases, the adsorbate state becomes a Lorentzian-shaped resonance within the adsorbent DOS, weakening antibonding contributions. Increasing V leads to a transition from resonance states to distinct bonding and antibonding states. If η_d shifts upward, bonding–antibonding splitting diminishes, and antibonding states become less populated enhancing adsorption.[41]

For transition metals, the d-band model offers a rationalization of trends in catalytic activity by a consideration of d-states alone, since their sp-bands are broad and uniformly filled. For example, when Cu d-states interact with nitrogen adsorbates, both bonding and antibonding states are filled, resulting in net repulsion. This repulsive interaction increases down the periodic table, explaining the weak adsorption on Au surfaces.[41]

For a recent discussion of current theoretical understanding of the OER at oxides more specifically, an extensive review has been provided by Jones *et al.*[42]

2.2 Proposed mechanisms and scaling relations

The OER exhibits inherently slow kinetics and has been studied extensively to optimise hydrogen production *via* water electrolysis. Understanding its mechanism is critical for rational catalyst design. Multiple mechanisms have been proposed, including those from Damjanovic and Bockris.[43,44] The OER is frequently discussed in terms of four proton-coupled electron transfers and typically involves two (oxide or electrochemical oxide path) or three (mononuclear path) intermediates. In acidic media at 25 °C, the reaction is:

$$2H_2O(l) \rightarrow O_2(g) + 4H^+ + 4e^- \quad (5)$$

$$\Delta G = 4.92 \text{ eV} = 474 \text{ kJ mol}^{-1}$$

One proposed pathway is the electrochemical oxide mechanism:[43]

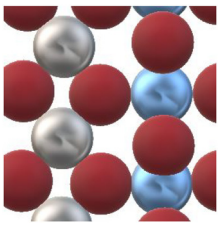

Fig. 5 Illustration of a single layer of CUS (silver) and bridge (blue) sites; red spheres represent oxygen.

$$* + H_2O(l) \rightleftharpoons OH_{ad} + H^+ + e^- \quad (6)$$

$$OH_{ad} \rightleftharpoons O_{ad} + H^+ + e^- \quad (7)$$

$$O_{ad} \rightleftharpoons \frac{1}{2}O_2(g) + * \quad (8)$$

where * is a surface active site and "ad" denotes adsorbed intermediates. Active sites can be metal sites, coordinatively unsaturated sites (CUS) or bridge sites. For metal oxides like RuO_2, CUS are atop fivefold Ru atoms, and bridge sites lie between fourfold coordinated Ru atoms.[45] These are illustrated in Fig. 5.

The oxide path is an alternative mechanism:[43]

$$* + H_2O(l) \rightleftharpoons OH_{ad} + H^+ + e^- \quad (9)$$

$$2OH_{ad} \rightleftharpoons O_{ad} + H_2O(l) + * \quad (10)$$

$$O_{ad} \rightleftharpoons \frac{1}{2}O_2(g) + * \quad (11)$$

In both paths, O–O bond formation arises from coupling of adsorbed oxygen. However, DFT calculations show this step has a high reaction barrier on metal surfaces, making it kinetically unfavourable.[46] An alternative is the mononuclear mechanism, where oxygen evolves *via* a hydroperoxo intermediate formed by nucleophilic attack of water on adsorbed oxygen.[45,47,48] Rossmeisl and Nørskov identified this step as rate-limiting.[46] They computed the free energies of each elementary step using:[46,49]

$$\Delta G(U, \text{pH}, p_{H_2} = 1 \text{ bar}, T) = \Delta G_0 + \Delta G_W + \Delta G_U + \Delta G_{field} + \Delta G_{pH} \quad (12)$$

where ΔG_0 is the equilibrium free energy, ΔG_W accounts for monolayer water effects, $\Delta G_U = -eU$ reflects potential bias, ΔG_{field} is the double-layer effect, and ΔG_{pH} corrects for proton activity. For metal oxides, ΔG_W and ΔG_{field} are often neglected.[45]

$$* + H_2O(l) \rightleftharpoons OH_{ad} + H^+ + e^- \quad (13)$$

$$\Delta G_1 = \Delta G_{OH_{ad}} - eU + k_B T \ln a_{H^+}$$
$$OH_{ad} \rightleftharpoons O_{ad} + H^+ + e^- \quad (14)$$

$$\Delta G_2 = \Delta G_{O_{ad}} - \Delta G_{OH_{ad}} - eU + k_B T \ln a_{H^+}$$
$$O_{ad} + H_2O(l) \rightleftharpoons OOH_{ad} + H^+ + e^- \quad (15)$$

$$\Delta G_3 = \Delta G_{OOH_{ad}} - \Delta G_{O_{ad}} - eU + k_B T \ln a_{H^+}$$
$$OOH_{ad} \rightleftharpoons O_2(g) + * + H^+ + e^- \quad (16)$$

$$\Delta G_4 = \Delta G_{O_2} - \Delta G_{OOH_{ad}} - eU + k_B T \ln a_{H^+}$$

For a perfect OER electrocatalyst, all four steps would have equal free energies (1.23 eV), totaling the theoretical value of 4.92 eV. However, in practice, one or two steps dominate due to larger energy barriers. While lowering the energy of these slow steps seems desirable, DFT studies by Nørskov's group revealed that the binding energies of OER intermediates scale linearly with one another, hindering independent optimization.[46] Man *et al.* showed that the difference between the binding energies OH_{ad} and OOH_{ad} is consistently 3.2 eV across oxides, implying that variations in overpotential from oxide to oxide are determined by the adsorption energy of oxygen. It also implies a universal overpotential limitation.[49] This relation is illustrated in Fig. 6, where an optimum oxygen binding energy of 1.67 eV results in all steps being downhill at 1.23 V, whereas a less optimal value of 2.3 eV places step 3 as rate-limiting a value relevant for pyrochlores (see Section 6.2).

Although breaking scaling relations appears beneficial, some studies show this does not always reduce overpotentials.[50] Since these relations are thermodynamic, Exner *et al.* argued that including kinetics may yield different design principles.[51] Nonetheless, Halck *et al.* demonstrated that incorporating Ni or Co into RuO_2 introduces proton donor–acceptor bridge sites that help decouple OH_{ad} and OOH_{ad} energies.[52] Introducing a hydrogen donor/acceptor has been widely used to circumvent adsorption scaling relations.[53]

Among the intermediates, O_{ad} is double-bonded, while OH_{ad} and OOH_{ad} are single-bonded to the surface. As a result, O_{ad} exhibits greater sensitivity to surface chemistry.[45] The OER rate thus correlates with the oxygen adsorption strength, producing a volcano-type relationship. Weak oxygen binding makes the formation of OH_{ad} (step 13) rate-limiting; strong binding shifts this to OOH_{ad} formation (step 15). Thus, oxygen binding energy serves as an effective descriptor for OER activity. Nørskov *et al.* also noted that oxygen evolution on metal surfaces requires an oxidized surface (Fig. 7).[46] In subsequent DFT work, rutile RuO_2 and IrO_2 were shown to outperform their reduced (metallic) counterparts due to their optimal O and OH binding energies.[45]

To advance electrocatalyst design, structure–property relationships must be better understood. Many studies introduce OER descriptors, properties correlating with activity, to aid catalyst screening. Often, plotting activity *versus* a descriptor forms a volcano plot. One example is the optimal filling of the e_g orbital,[54] linked to the binding strength of OER intermediates highlighting the central role of adsorption.

2.3 Lattice oxygen participation

The oxygen evolution reaction (OER) does not always follow straightforward adsorption pathways. The typical scaling relations based on intermediate binding energies can sometimes be bypassed *via* an alternative mechanism known as the lattice oxygen mechanism (LOM), where lattice oxygen participates directly in oxygen evolution. This behaviour has been observed in iridium- and ruthenium-based oxides,[55,56] as well as in ternary oxides like perovskites, helping to lower overpotentials.[57]

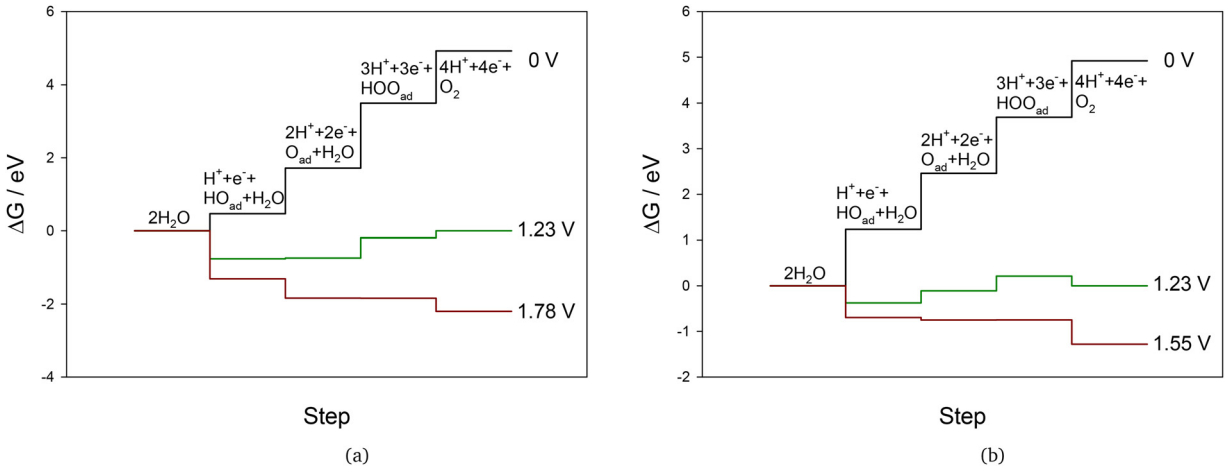

Fig. 6 (a) Free energy diagram for an oxygen binding energy of 1.67 eV, corresponding to the computed binding energy for iridium oxide.[45] Curves for 0.0 V, 1.23 V, and 1.78 V, are shown as indicated. pH = 0. (b) Free energy diagram for an oxygen binding energy of 2.3 eV, corresponding to the computed binding energy that gives the minimum overpotential.[45] Curves for 0.0 V, 1.23 V, and 1.55 V, are shown as indicated. pH = 0. All curves were calculated from equations provided by Rossmeisl *et al.*[45]

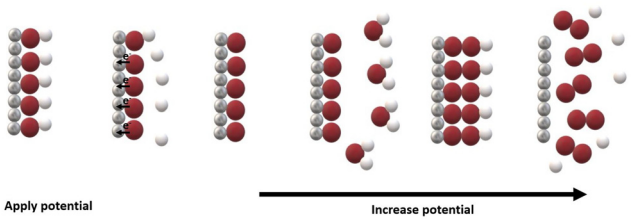

Fig. 7 OER mechanism as described by Rossmeisl and Nørskov.[46] Silver: metal surface; red: oxygen; white: hydrogen. When a potential is applied, water molecules dissociate and form OH_{ad} (eqn (13)). Without a further increase in potential, a proton is split off into solution and an electron to the electrode (eqn (14)). After this, the coverage of O_{ad} increases until no new OH_{ad} forms. If the potential is high enough, water molecules will adsorb on O_{ad}, forming OOH_{ad} (eqn (15)) and eventually evolve O_2 (eqn (16)).

Interest in LOM grew when certain perovskites outperformed others predicted to be optimal by volcano plots based on the adsorbate evolution mechanism (AEM).[54,58] While the AEM-based volcano is largely universal for perovskites, LOM depends on A-site identity.[57] Furthermore, it has been validated through both DFT simulations[59,60] and isotope labeling experiments.[61] Rong *et al.* proposed that LOM proceeds *via* reversible formation of surface oxygen vacancies (V_O), as shown below:[57,60]

$$OH_{ad} \rightleftharpoons (V_O + OO_{ad}) + H^+ + e^- \quad (17)$$

$$(V_O + OO_{ad}) + H_2O \rightleftharpoons O_2 + (V_O + OH_{ad}) + H^+ + e^- \quad (18)$$

$$(V_O + OH_{ad}) + H_2O \rightleftharpoons (H_{O\text{-site,ad}} + OH_{ad}) + H^+ + e^- \quad (19)$$

$$(H_{O\text{-site,ad}} + OH_{ad}) \rightleftharpoons OH_{ad} + H^+ + e^- \quad (20)$$

As in AEM, the first step involves OH adsorption. Deprotonation triggers lattice O to participate, forming OO_{ad} and leaving behind V_O. O–O bond formation occurs *via* O migration to a bridge site. Oxygen is evolved in the second step, and OH^- refills the vacancy in step 3, protonating adjacent lattice oxygen due to the B-sites limited ability to donate electrons to undercoordinated surface oxygens. When bulk oxygen vacancies exist, LOM can bypass earlier steps and proceed from eqn (19).[60]

Tuning the B-site valence in ternary oxides can promote LOM by facilitating V_O formation, which becomes thermodynamically favourable as the B–O bond weakens.[60] Lower catalyst stability increases surface protonation, introducing new LOM-specific scaling relationships, particularly between OH_{ad} and OO_{ad} (with a typical $\Delta G \approx 1.4$ eV for La-based perovskites),[57] in contrast to the OH_{ad}–OOH_{ad} pair in AEM. Some variants that also involve double-bonded O intermediates have been suggested as well.[62] Notably, LOM dominates both the weak-binding leg and the top of the volcano trend in some systems.[57] Finally, it is important to note that proton and electron transfers are not necessarily always concerted.

2.4 The OER mechanism of pyrochlores

Early work by Horowitz *et al.* showed that Bi- and Pb-based ruthenate pyrochlores were active for electro-oxidative C–C bond cleavage and proposed a similar cyclic Ru–O intermediate for the OER (Fig. 8).[4,63] This may also explain the absence of hydrogen peroxide in the ORR and the higher activity toward OER. Shortly after, Goodenough *et al.* reported that the active site in $Pb_2(M_{2-x}Pb_x)O_{7-y}$ (M = Ru or Ir) is a surface O^-, stabilised by oxidation of redox couples near the top of the O^{2-}:$2p^6$ valence band.[64] The redox pairs Ru^{5+}/Ru^{4+} and Ir^{5+}/Ir^{4+} fulfil this. For $Pb_2Ir_2O_7$, surface protonation is influenced by pH, with O′ sites protonated below the isoelectric point (pH 3.3). They proposed two mechanisms based on protonation state: At low pH (pH < 1.5):

$$Ru^{4+}OH^- \rightarrow Ru^{5+}O^{2-} + H^+ + e^- \quad (21)$$

$$Ru^{5+}O^{2-} \rightleftharpoons Ru^{4+}O^- \quad (22)$$

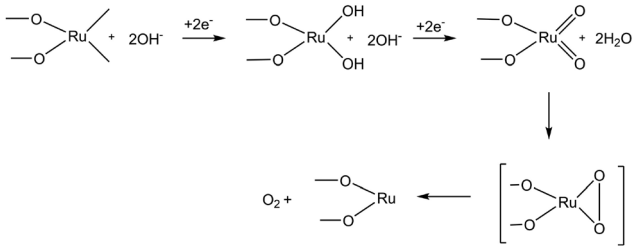

Fig. 8 Proposed cyclic Ru–O intermediate in the OER on ruthenate pyrochlores. Adapted from Horowitz *et al.*[4,63]

$$Ru^{4+}O^{-} + H_2O \rightarrow Ru^{4+}OOH^{-} + H^{+} + e^{-} \quad (23)$$

$$2Ru^{4+}OOH^{-} \rightarrow 2Ru^{4+}OH^{-} + O_2\uparrow \quad (24)$$

At higher pH ($1.5 < pH < 3.3$), involving O′ proton donors:

$$Ru^{4+}O^{2-} + Pb^{2+}OH_2 \rightarrow Ru^{5+}O^{2-} + Pb^{2+}OH^{-} + H^{+} + e^{-} \quad (25)$$

$$Ru^{5+}O^{2-} \rightleftharpoons Ru^{4+}O^{-} \quad (26)$$

$$Pb^{2+}OH^{-} + Ru^{4+}O^{-} + H_2O \rightarrow Ru^{4+}OO^{2-} + Pb^{2+}OH_2 + H^{+} + e^{-} \quad (27)$$

$$2Ru^{4+}OO^{2-} \rightarrow 2Ru^{4+}O^{2-} + O_2\uparrow \quad (28)$$

These steps are widely cited as the most detailed OER mechanisms for Ru/Ir pyrochlores.[65–69] Prakash *et al.* also studied $Pb_2Ru_2O_{6.5}$, reporting that both surface and bulk contribute to OER, based on cyclic voltammograms (CVs) correlated with BET surface area.[70] Their mechanism suggests first-order dependence on [OH^-] in alkaline media (pH 11–14), with contributions from both Ru and Pb oxidation (Fig. 9).

In a later study,[71] they reaffirmed first-order [OH^-] dependence and proposed that the second electron transfer is rate-limiting. Their model includes adjacent Ru–OH sites on the (111) surface and the formation of a seven-coordinate Ru^{5+} (Fig. 10), similar to a previously reported additional

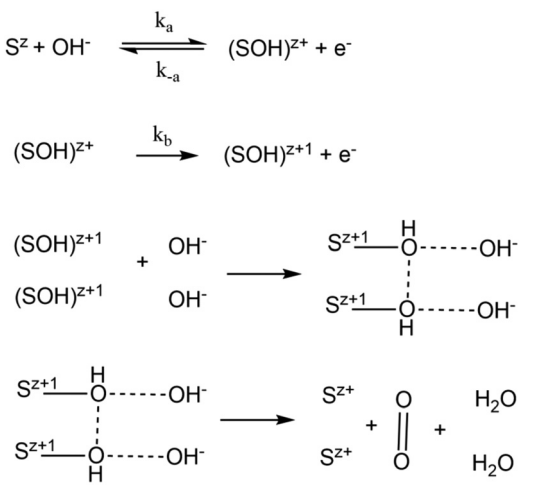

Fig. 9 OER mechanism on Pb–Ru pyrochlore. S denotes an active site.[70]

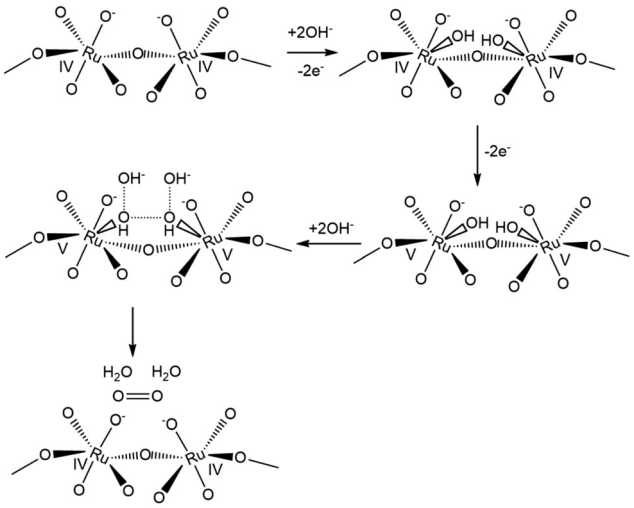

Fig. 10 Detailed OER mechanism with formation of seven-coordinate Ru^{5+}. Used with permission of IOP Publishing Limited, from Journal of the Electrochemical Society, Prakash *et al.*[86], 1948; permission conveyed through Copyright Clearance Center, Inc.

electron-transfer step preceding OOH formation.[47] Unlike Horowitz's single-site model, OH and O are adsorbed on adjacent Ru sites. Sardar *et al.* investigated $Bi_2Ru_2O_7$ and suggested that the mechanism resembles that of RuO_2 or IrO_2, though direct comparison is difficult due to structural differences.[66] Parrondo *et al.* studied lead-based pyrochlores (Ru, Ir, Os) and proposed an AEM-type pathway involving oxygen intermediates bonded to B-sites. OER activity was found to increase with Ru content, attributed to stronger B–O bonding. The mechanism involves four electron transfers, with O–O bond formation and proton removal as rate-limiting steps (see Fig. 11).[72] Several studies report AEM-type mechanisms for Ru- and Ir-based pyrochlores.[20,29,73–75] Kim *et al.* proposed an AEM pathway involving a transient Ru^{6+} species in acidic media for $Y_2Ru_2O_7$:

$$Ru^{+4} + 2H_2O \rightarrow Ru^{+5}OH + H_2O + H^{+} + e^{-} \quad (29)$$

$$Ru^{+5}OH + H_2O \rightarrow Ru^{+6}O + H_2O + H^{+} + e^{-} \quad (30)$$

$$Ru^{+6}O + H_2O \rightarrow Ru^{+5}OOH + H^{+} + e^{-} \quad (31)$$

$$Ru^{+5}OOH \rightarrow Ru^{+4} + O_2 + H^{+} + e^{-} \quad (32)$$

Feng *et al.* applied this mechanism to $Y_{1.85}Ba_{0.15}Ru_2O_{7-y}$,[68] while earlier proposing an electrochemical oxide path for Zn-doped analogues,[67] involving adjacent adsorbed O atoms forming O–O bonds. Zhou *et al.* presented a related mechanism on mixed A-site pyrochlores (Fig. 12).[76] Lattice oxygen involvement (LOM-type mechanisms) in pyrochlores was suggested more recently,[62,77–79] and remains less frequently reported than surface-adsorbed oxygen pathways. It is likely that different pyrochlores follow different mechanisms, but consensus is lacking. Further *in situ* studies, such as isotope labelling with differential electrochemical mass spectrometry (DEMS), are needed to confirm LOM activity, as demonstrated by Abbott *et al.*[75]

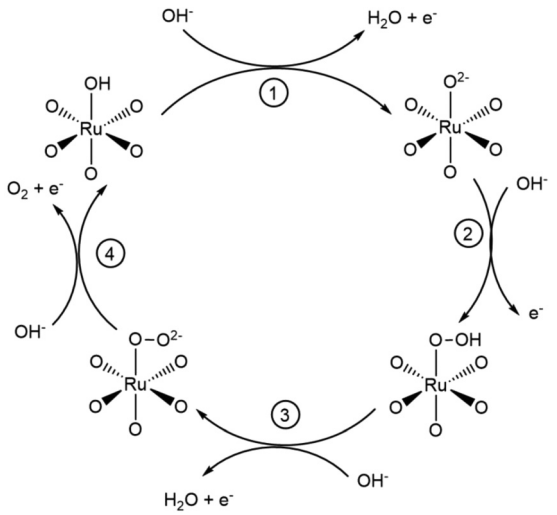

Fig. 11 OER mechanism on lead ruthenate pyrochlores in alkaline media, redrawn with permission from Parrondo *et al.*[72] Copyright Royal Society of Chemistry 2015.

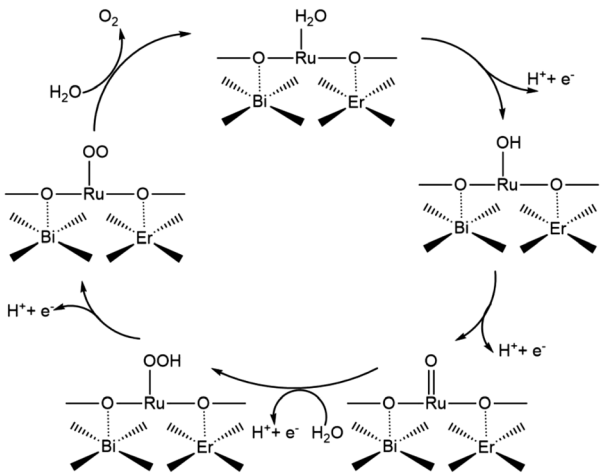

Fig. 12 Illustrated OER pathway in a Bi/Er co-doped pyrochlore. Redrawn from Zhou *et al.*[76]

2.5 Does the A-site contribute to electrochemical activity?

In pyrochlores, the A-site is traditionally considered inert, but its participation has been increasingly implicated in OER performance. Goodenough and ten Kortenaar *et al.* suggested A-site involvement.[64,65] Redox behaviour in Eu-based iridates (Eu^{3+}/Eu^{2+}) offers an added conduction pathway.[65] They also linked visible A-site redox peaks in CVs to enhanced activity (Section 5.2).[65] More recently, Park *et al.* used *in situ* XAS to show that in $Y_2(Ru_{2-x}Y_x)O_{7-y}$, both Ru and Y undergo oxidation, providing additional electron channels during OER.[77] Similarly, in $Tl_2Rh_2O_7$, simultaneous oxidation of A- and B-sites improved charge transport and boosted activity.[80] Such findings are especially relevant in bifunctional catalysts (OER and ORR), emphasizing that the A-site should not be assumed inert.[65,77,80]

3 Pyrochlores as heterogeneous catalysts and their electrocatalytic properties towards the oxygen evolution reaction (OER)

Ruthenate pyrochlores have been studied as OER electrocatalysts since the early 1980s, with their activity typically attributed to the variable oxidation states of Ru.[4,14,71,81–83] Tables 1–3 summarise reported cases of ruthenate (and iridate) pyrochlores used for the OER. It includes synthesis methods, physical characteristics, OER activity (as overpotential at 10 mA cm^{-2}), and the electrolyte used. The entries are listed chronologically, and where applicable, the most active or relevant catalyst from each study is selected. For studies using multiple synthesis temperatures, the highest calcination temperature is noted. Both acidic and alkaline OER catalysts are included. The table highlights the wide range of modification strategies available to tune pyrochlore OER activity. A- and B-site cations can be varied or doped to alter the structure. The B-site, typically occupied by Ru or Ir, is the active site for OER, while the A-site can host alkaline earths, lanthanides, or basic metals. The following sections explore these modifications in detail.

3.1 Changing the A-site cation

As shown in Tables 1–3, over 16 different elements, including Pb, Bi, Na, Ce, Y, Tl, Pr, Yb, Gd, Nd, Ho, Er, Dy, Sm, Lu, and Co, have been used as A-cations in ruthenate and iridate pyrochlores. These include lanthanides, transition metals, alkali metals, and other metals. The A-site cations size, electronegativity, spin–orbit coupling, and valence state have all been reported to influence electrocatalytic activity. Trends related to these properties are discussed in this section.

The earliest pyrochlores used for the oxygen evolution reaction (OER) featured Pb or Bi at the A-site ($Bi_2Ru_2O_7$ and $Pb_2Ru_2O_7$).[4,63,64,66,70–73,83–85] Ruthenium-deficient variants, where Pb or Bi partially occupy B-sites, have shown higher OER activity than noble metals.[21] These materials have primarily been studied in alkaline media, where they outperform their performance in acidic environments. Most early studies also report better OER than ORR activity. In 2017, research interest shifted toward Y-containing pyrochlores.[20,67,77,89,90,97,98] Yttrium-based ruthenate pyrochlores demonstrate good performance in both acidic and alkaline media.[20,74] According to Tables 1–3, Y is among the most frequently used A-site cations in OER-active pyrochlores.

3.1.1 Ionic radius of the A-cation. For ionic radii values, we recommend the use of Shannon radii, which is also what is used in this review.[130] There is conflicting information in the literature regarding the correlation between the A-site cation radius and OER activity. Some studies report enhanced OER activity and stability with decreasing A-site ionic radius,[75,102,121] while others find the opposite.[92,120] Some observe non-monotonic "zigzag" trends,[126] or report similar activities for cations with comparable radii.[99] Notably, Park *et al.* found

Table 1 Pyrochlores employed as OER electrocatalysts

Pyrochlore	Synthesis method, calcination temperature	Particle size (nm)	Surface area (m^2 g^{-1})	Overpotential (mV at 10 mA cm^{-2})	Electrolyte
$Pb_2(Ru_{2-x}Pb_x)O_{6.5}$ $Bi_2(Ru_{2-x}Bi_x)O_{6.5}$[4,63]	Alkaline solution	—	50–200	140	3 M KOH
$Pb_2(M_{2-x}Pb_x)O_{7-y}$ (M = Ru or Ir)[64]	Direct solid-state, 850 °C	—	—	0.72 V *vs.* Hg/$HgSO_4$	2.5 M H_2SO_4
$Pb_2Ru_2O_{6.5}$[70]	Alkaline solution		6		1 M KOH
$Bi_2Ru_2O_7$[84]	Solid state, 1000 °C				2.5 M H_2SO_4
$Pb_2(Ir_{2-x}Pb_x)O_{7-y}$[65]	Solid-sate, 825 °C			−20 mV *vs.* SSE	KOH
$Bi_2Ru_2O_7$ and $Pb_2Ru_2O_{6.5}$[85]	Solid state				1 M KOH
$Pb_2(Ru_{2-x}Pb_x)O_{6.5}$[71]	Alkaline solution	—	35–55	—	5.5 M KOH
$Pb_2Ru_2O_{6.5}$[86]	Alkaline solution				1 M KOH
$Bi_2Ru_2O_7$[83]	Pechini	500	2	—	1 M KOH
$Bi_2Ir_2O_7$[66]	Hydrothermal	10	46	370	1 M H_2SO_4
$(Na_{0.33}Ce_{0.67})_2Ru_2O_7$[87]	Hydrothermal	38	60–80	214	MEA
$Pb_2Ru_2O_{6.5}$	Alkaline solution and/or solid-state	50–100	100	210	0.1 M KOH
$Bi_{2.4}Ru_{1.6}O_7$[72]			7.8	370	
$Bi_2Ir_2O_7$ $Pb_2Ir_2O_{6.5}$[73]	Hydrothermal	20–50	14.8	Did not reach	0.1 M $HClO_4$
$Bi_2Ru_2O_7$[88]	Alkaline solution	—	—	—	0.1 M KOH
$Pb_2Ru_2O_{6.5}$	Sol–gel (CA), 650 °C	≤200	—	410	0.1 M KOH
$Sm_2Ru_2O_7$[74]			—	448	
$BiYIr_2O_{6.5+x}$[89]	Adams fusion	10–200	40	—	0.1 M $HClO_4$
$Y_2(Ru_{2-x}Y_x)O_{7-y}$[77]	Sol–gel (CA), 1050 °C	200	4.26	490	0.1 M KOH
$Y_2Ru_2O_{7-\delta}$[20]	Sol–gel (A), 1000 °C	>200	7.22	190	0.1 M $HClO_4$
$Y_2Ir_2O_7$[90]	Sol–gel (CA), 1000 °C	150	7.3	—	0.1 M $HClO_4$
$Tl_2Rh_2O_7$[80]	Sol–gel type	<200	—	395	0.1 M KOH
$Y_2(Ru_{1.6}Y_{0.4})O_{7-y}$[91]	Sol–gel + porogen	10	33.3	250	0.1 M $HClO_4$
$Pr_2Ir_2O_7$[92]	Sol–gel (CA), 900 °C	>200	1.55	295	0.1 M $HClO_4$
$Y_{1.85}Zn_{0.15}Ru_2O_{7-\delta}$[67]	Sol–gel (CA), 1050 °C	>300	4.2	291	0.5 M H_2SO_4
$Yb_2Ru_2O_7$	Spray-freeze	83	—	21 mA cm^{-2}	0.1 M $HClO_4$
$Gd_2Ru_2O_7$	Freeze-dry, 1200 °C	173		19.9 mA cm^{-2}	
$Nd_2Ru_2O_7$[75]		350		12.1 mA cm^{-2} at 350 mV	
$Tl_2Ru_2O_7$ + surface PO_4^{3-} (ref. 93)	Sol–gel, 1200 °C	<200	5.24	270	0.1 M KOH
$Y_2Ru_{2-x}Co_xO_7$[94]	Sol–gel, 1350 °C + *in situ* exsolution of Co	500		250	0.1 M KOH
$Y_{1.85}Ba_{0.15}Ru_2O_{7-\delta}$[68]	Pechini, 1050 °C	>100	16.4	278	0.5 M H_2SO_4
$Pb_2Ru_2O_{7-x}$[95]	Alkaline solution	70–140		500	0.6 M NaCl and $NaClO_4$
$Pb_2Ru_2O_{7-x}$[96]	Alkaline solution, varying temperatures and atmospheres	105 ± 35	85	200	0.1 M KOH
$Y_{1.75}Ca_{0.25}Ru_2O_{7-\delta}$[97]	Pechini, 1100 °C	>300	7.9	275	0.5 M H_2SO_4
$Y_2Ru_2O_{7-\delta}$[98]	Polymer entrapment flash pyrolysis (PEPF), 550 °C	40	14.8	280	0.1 M $HClO_4$

drastically different activities in pyrochlores with nearly identical A-cation sizes (Pb: 1.29 Å *vs.* Sm: 1.27 Å).[74]

Liu *et al.* reported increasing activity with increasing A-site radii from Yb to Nd (Fig. 13).[102] Similar trends were observed with A-cations from Ho (1.015 Å) to Pr (1.126 Å).[92,112] Celorrio *et al.* also found Dy_2RuMnO_7 to outperform smaller-radius analogues.[100]

Conversely, Abbott *et al.* observed increasing activity with decreasing A-cation size in $A_2B_2O_7$ (A = Nd, Gd, Yb; B = Ru, Ir), following Yb → Gd → Nd.[75] Hubert *et al.* reported similar findings, although differences were marginal among Y, Nd, and Gd.[99] Bi-containing pyrochlores performed worse, but this may stem from Bi's unique electronic configuration rather than size alone.[99] Yin *et al.* also found activity decreased with increased size from Nd to Ho.[121]

Early work by ten Kortenaar *et al.* showed the trend Pb (1.29) > Eu (1.066) > Nd (1.109) > Bi (1.17), with no clear correlation to A-site radius.[65] Recently, Guo *et al.* performed a comprehensive study across lanthanide ruthenate pyrochlores (Sm–Lu) and found Tb in the A-site to be most active.[126] Larger-radius cations (La, Ce, Pr, Nd) couldnt form phase-pure pyrochlores. They reported an activity increase with increasing radius up to Tb, then a decline (Gd, Eu, Sm).[126] In other words, they found a volcano-type correlation. This shows that certain elements in the lanthanide series may appear to have increasing activities as the radius increases while others will show the opposite trend. This could potentially explain conflicting trends in the literature.

3.1.2 The fourth ionization energy. Instead of ionic radius, Guo *et al.* proposed the fourth ionization energy (I_4) of the

Table 2 Pyrochlores employed as OER electrocatalysts continued

Pyrochlore	Synthesis method, calcination temperature	Particle size (nm)	Surface area ($m^2\ g^{-1}$)	Overpotential (mV at 10 mA cm^{-2})	Electrolyte
$Y_2Ru_2O_{7-\delta}$	Sol–gel (CA), 1000 °C	>100	28.8	360	0.5 M H_2SO_4
$Y_{1.8}Cu_{0.2}Ru_2O_{7-\delta}$			7.9	360	
$Y_{1.8}Co_{0.2}Ru_2O_{7-\delta}$			9.0	n.a.	
$Y_{1.8}Ni_{0.2}Ru_2O_{7-\delta}$			12.8	n.a.	
$Y_{1.8}Fe_{0.2}Ru_2O_{7-\delta}$[62]			13.9	410	
$Y_2Ru_2O_7$	Sol–gel (CA), 1000 °C	>100	2.7	331	0.1 M $HCLO_4$
$Nd_2Ru_2O_7$			2.3	346	
$Gd_2Ru_2O_7$	700 °C (for Bi)		2.0	360	
$Bi_2Ru_2O_7$[99]			4.4	358	
Dy_2RuMnO_7	Sol–gel (CA), 900 °C	60	4.5	—	0.1 M KOH
Ho_2RuMnO_7					
Er_2RuMnO_7[100]					
$Yb_2(Ru_{0.58}Ir_{0.42})_2O_7$[101]	SF-FD, 1020 °C	100	—	250	0.1 M $HCLO_4$
$Nd_2Ru_2O_7$	Sol–gel (CA), 1000 °C	100–200	—	310	0.1 $MHClO_4$
$Sm_2Ru_2O_7$				350	
$Er_2Ru_2O_7$				—	
$Yb_2Ru_2O_7$[102]				—	
$Y_2Ru_{1.9}Mn_{0.1}O_{7-\delta}$	Sol–gel, 1050 °C	>200	7.02	256	0.5 M H_2SO_4
$Y_2Ru_{1.9}Fe_{0.1}O_{7-\delta}$[103]			7.14	273	
$Y_{1.7}Sr_{0.3}Ru_2O_7$[29]	Sol–gel (CA), 900 °C	>200	4.98	264	0.5 M H_2SO_4
$Lu_2Ir_2O_7$[104]	Hydrothermal	—	—	305	0.1 M $HClO_4$
$Y_2Ru_2O_{7-\delta}F_x$[79]	Sol–gel (CA) + fluorination	>50	90.08 (ECSA)	235	0.5 M H_2SO_4
$(CaNa)_2Ir_2O_6{\cdot}nH_2O$	Hydrothermal	10–40	62.7	8.31 mA cm^{-2}	MEA
$Ca_2Ir_2O_6{\cdot}nH_2O$			26.2	5.42 mA cm^{-2}	
$(CaNa)_2IrRuO_6{\cdot}nH_2O$[69]			33.5	8.24 mA cm^{-2} at 270 mV (BET)	
$Bi_2Ru_2O_7$[105]	Sol–gel, 1050 °C	>900	—	535	0.1 M KOH
$Y_2Ru_2O_{7-\delta}$[78]	Sol–gel autocombustion, 1100 °C, quenching	<100	15.6	241	0.1 M $HCLO_4$
$Y_2Ir_2O_7$[106]	Adams funsion	50	22	417	0.5 M H_2SO_4
$Pr_{1.8}Zn_{0.2}Ir_2O_7$	Hydrothermal	119.7	5	340	0.1 M $HCLO_4$
$Lu_{1.8}Zn_{0.2}Ir_2O_7$[107]		654.17	9.2	331	
$Ho_2Ru_2O_7$[108]	Electrospinning, 900 °C	50	8.85	280	0.1 M $HCLO_4$
Y_2MnRuO_7[109]	Sol–gel (CA), 1000 °C	50	—	300	0.1 M $HCLO_4$
$Y_2Ru_{1.2}Ir_{0.8}O_7$[110]	Sol–gel (CA), 1000 °C	>300	—	220	0.5 M H_2SO_4
$Bi_xEr_{2-x}Ru_2O_7$[76]	Sol–gel (CA) with perchloric acid, 1000 °C	—	—	180	0.1 M $HCLO_4$
$Bi_2Ru_2O_7$ on $Bi_2Ti_2O_7$[111]	Alkaline solution + epitaxial growth	100	—	270	0.1 M KOH
Pr_2RuIrO_7[112]	Amino-acid aided synthesis, 1050 °C	400–500	—	350	1 M KOH
$Bi_{1.68}Co_{0.32}[Nb_{1.4}Co_{0.6}]O_{7-\delta}$[113]	Sol–gel auto-combustion, 950 °C	—	—	300	1 M KOH
$Pb_2[Ru_{2-x}Pb_x]O_{7-\delta}$[114]	Low-temperature pyrolysis cation exchange resin (CER), 350 °C	40–100	44.2	174	0.1 M $HCLO_4$

lanthanides as a material property that scales with OER activity.[126] I_4 indicates how easily the lanthanide is oxidized (Ln^{3+}/Ln^{4+}), with activity increasing with ease of oxidation (decreased I_4). They predicted that $Pr_2Ru_2O_7$ would exhibit excellent activity due to its low I_4.[126] Zhan *et al.* later synthesized this pyrochlore and confirmed its high activity.[120] Similarly, $Pr_2Ir_2O_7$ has been synthesized and was found to be the top performer among lanthanide iridate pyrochlores in two studies.[92,112] These observations support the hypothesis that the A-site cation influences electron transfer (Section 2.5).

However, not all results align with this trend. Shang *et al.* found that $Nd_2Ir_2O_7$ and $Gd_2Ir_2O_7$ outperformed $Tb_2Ir_2O_7$, despite Tb having a lower I_4, though $Pr_2Ir_2O_7$ remained the best.[92] If I_4 were a reliable predictor, Ce in the A-site should show high activity due to its low I_4. However, Ce predominantly exists in the +4 state and has only been synthesised as $(Na_{0.33}Ce_{0.67})_2Ru_2O_7$, likely to maintain charge balance.[87] Overall, no universal correlation exists between A-site size or I_4 and OER activity. Nevertheless, both clearly influence activity, likely through other size-dependent or electronic structure-related properties.

3.1.3 The effect of the A-site on coordination geometry. The size of the A-cation influences the B-site coordination geometry by distorting the BO_6 octahedra, which in turn affects the electronic structure through mechanisms such as spin–orbit coupling (SOC). The superior activity of iridate pyrochlores (with various A-cations) over rutile IrO_2 has been attributed to stronger SOC.[90,92]

In IrO_2, electrons adopt a low-spin state, leading to filled t_{2g} and empty e_g orbitals in a perfect octahedron.[90,92] However, some report distorted octahedra and a splitting of the t_{2g} $\left(J=\frac{5}{2}\right)$ orbitals, resulting in filled u′ $\left(J=\frac{3}{2}\right)$ subbands and a half filled e″ $\left(J=\frac{1}{2}\right)$ subband (Fig. 14).[73,131] Sun *et al.* observed a shoulder near E_F in the XPS valence band spectrum of IrO_2 and $Bi_2Ir_2O_7$, attributed to this splitting.[73] Shih *et al.* and Shang *et al.* also reported this effect in iridate pyrochlores

Table 3 Pyrochlores employed as OER electrocatalysts continued

Pyrochlore	Synthesis method, calcination temperature	Particle size (nm)	Surface area (m^2 g^{-1})	Overpotential (mV at 10 mA cm^{-2})	Electrolyte
$Y_2Ru_{2-x}Ti_xO_7$[115]	Sol–gel (CA), 900 °C	100–200	—	229	0.5 M H_2SO_4
$Y_{1.75}Co_{0.25}Ru_2O_{7-\delta}$[116]	Sol–gel, 1100 °C, ball-milled	400	—	275	0.5 M H_2SO_4
Y_2MnRuO_7[117]	Citrate, 900 °C	60	0.6 (incl. vulcan, ECSA)	270	0.1 M $HCLO_4$
$Co_2Sb_2O_7$[118]	Solid-state, 450 °C	100–500	68.7	288	0.5 M H_2SO_4
$Y_2Ru_2O_{7-\delta}$ + MoO_x modifiers[37]	Sol–gel + porogen wet chemical peroxone	>100	11.58	240	0.1 M $HCLO_4$
$Y_2Ru_2O_7$ with P-doped Ru on the surface[119]	Sol–gel (CA), exsolution and pyrolysis	—	186.1	232	1 M KOH
$Pr_2Ru_2O_7$[120]	Sol–gel (CA), 950 °C	>500	6.64	213	0.5 M H_2SO_4
$Ho_2Ru_2O_7$[121]	Electrospinning, 900 °C	50	—	280	0.1 M $HCLO_4$
$Y_{1.6}Pb_{0.4}Ru_2O_{7-\delta}$[122]	Sol–gel (CA) + porogen	—	18.77	195	0.1 M $HCLO_4$
$Na_xGd_{2-x}Ru_2O_{7-\delta}$[123]	Sol–gel (CA), 900 °C	110	4.07	260	0.1 M $HCLO_4$
$Mn_2P_2O_7$ and graphene nanosheets composite[124]	Hydrothermal, 400 °C + ultrasonication	12.98	—	240	1 M KOH
$Y_2Ru_2O_7$ support for NiFe/Ru-PS[125]	Sol–gel (CA)	—	100	241	1 M KOH
$Ln_2Ru_2O_7$, Ln = Sm to Lu[126]	Sol–gel (CA) + perchloric acid, 900 °C or 1050 °C	70	6	218–240	0.1 M $HCLO_4$
$Y_2Ru_{1.9}Sr_{0.1}O_7$[127]	Sol–gel (CA), 1000 °C	50	9.75	228	0.5 M H_2SO_4
$Y_2Ru_2O_7S_0.17$[128]	Hydrothermal	30	12.91	237	0.5 M H_2SO_4
$Y_2Ru_{2-x}Pd_xO_7$[129]	Sol–gel (CA)	200–300		260	1 M KOH

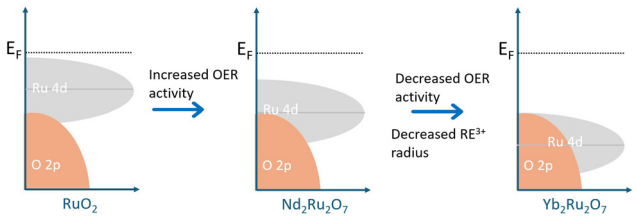

Fig. 13 A schematic illustration of the rigid band structures for RuO_2, $Yb_2Ru_2O_7$ and $Nd_2Ru_2O_7$ redrawn with permission from Liu *et al.*[102] Copyright Springer Nature 2021.

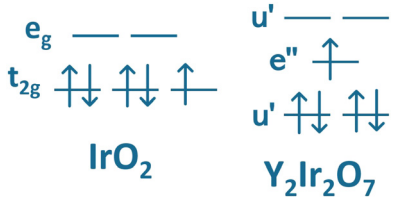

Fig. 14 An illustration of the orbital filling in IrO_2 and $Y_2Ir_2O_7$.[90]

and linked the enhanced OER activity to the single-electron-filled e″ subband.[90,92]

Conversely, Sun *et al.* suggested that SOC is not present in distorted IrO_6 octahedra, causing the disappearance of the $J = \frac{1}{2}$ subband.[73] They correlated this to the superior activity of $Pb_2Ir_2O_{6.5}$ over $Bi_2Ir_2O_7$ and IrO_2.[73] Nonetheless, they observed further splitting of $J = \frac{3}{2}$, leaving one half-filled orbital. This e″ orbital in pyrochlores may thus mimic the half-filled e_g orbital in perovskites/TMOs, known for optimal binding strength in OER catalysis.[54] This so-called "single electron in a single orbital" (SESO) configuration helps explain the generally high OER activity of iridate pyrochlores but offers limited guidance for designing new compositions. Additionally, strong electron correlations in some $RE_2Ir_2O_7$ pyrochlores lead to $J = \frac{1}{2}$ splitting into upper and lower Hubbard bands.[92] As the RE radius increases, electron correlations weaken, shrinking this gap and enhancing conductivity (Fig. 15).[92] Therefore, pyrochlores may become more conductive as the A-site increases in size.

3.1.4 The effect of the A-site on B–O covalency. As we touched upon, the A-cation size, and thus the degree of distortion of the BO_6 octahedra, also influences B–O bond covalency.[74] It is often reported that the A-cation affects the overlap between the B-site d-orbitals and O 2p orbitals, thereby impacting B–O bond length. However, no consistent correlation between A-site ionic radius and Ru–O bond length has been established.[99]

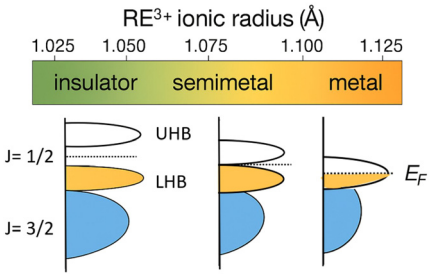

Fig. 15 A schematic illustration of the band structures of Ir 5d orbitals of rare-earth (RE) iridate pyrochlores and the corresponding phase diagram. Used with permission of John Wiley & Sons, from ref. 92; permission conveyed through Copyright Clearance Center, Inc.

In some cases, increasing the A-site radius reduces B–O bond strength, which corresponds to higher oxygen vacancy concentrations.[7,132] Liu *et al.* used this reasoning to ascribe increased OER activity to larger A-site cations (Fig. 13).[102] In contrast, Shang *et al.* reported a positive correlation between Ir–O bond covalency and OER activity, associated with increasing A-cation size (Fig. 15).[92] Other studies found that stronger Ru–O bonds, occurring with decreasing A-site radius, enhance activity.[99]

There is clear disagreement on whether longer or shorter B–O bonds favour OER activity. The majority of the publications on pyrochlore OER electrocatalysts claim shorter bonds (stronger p–d hybridization) lead to increased OER activity,[20,73,74,92,93,95,96,100,104,108,117] while some find the opposite to be true.[20,75,78,99,102,106,120,121]

Changes in A-site cation also influence the relative positions of the Ru 4d/Ir 5d and O 2p band centers. DFT calculations have showed that increased distortion in IrO_6 octahedra leads to broader d-band widths and thus greater Ir 5d–O 2p band overlap.[73] Ru–O bond lengths likewise affect the d-band center in ruthenate pyrochlores, though conflicting reports exist: some find that shorter Ru–O bonds downshift the d-band center,[20,117] while others claim that longer bonds cause this downshift and optimise the binding energy of oxygen intermediates.[120]

Larger overlap of Ru–O/Ir–O orbitals are said to increase the O 2p band center converting from AEM to LOM.[104] Higher O 2p band centers allow more of the d-band to enter into the O 2p band.[104] A downshift of the d-band center in acidic media may lead to increased OER activity.[104]

3.1.5 The role of electronegativity. The ionic radius influences the electronegativity. The electronegativity of the A-site cation affects B–O bond covalency. When A- and B-site cations have similar electronegativities, greater covalency is expected between B–O–B and A.[5,93] As a result, it is common practice in pyrochlore design to select A- and B-cations with similar electronegativities. For example, Kim *et al.* used Tl and Rh (for which they report Pauling electronegativities of 2.04 and 2.28, respectively) to promote covalent Rh–O–Rh/Tl bonding, favouring electron delocalisation.[80] It should be noted that the electronegativity of Tl is reported as 1.8 in the CRC Handbook of Chemistry and Physics.[133] When the A-cation is much less electronegative than the B-cation, the metal–oxygen bond becomes more ionic, increasing the band gap and causing insulating behaviour.[5,92] Park *et al.* emphasised this concept by showing that Ru–O–Ru/Pb bonding is more covalent than Ru–O–Ru/Sm, due to the closer electronegativities of Ru (2.2) and Pb (2.33), compared to Sm (1.17).[74] They further linked higher Ru–O bond covalency to better alignment of A- and B-site e_g state Fermi energies. Specifically, $Pb_2Ru_2O_{6.5}$ showed stronger covalent bonding than $Sm_2Ru_2O_7$ due to the proximity of Pb 6p and Ru 4d orbital energies, in contrast to the more distant Sm 4f levels.[74]

Electronegativity also affects OER activity independently of ionic radius. Yan *et al.* substituted Ho (for which they provide an electronegativity 1.377) for Y (for which they provide an electronegativity 1.291) in $Y_2Ru_2O_7$ and attributed improved activity to the higher electronegativity of Ho, which resulted in larger Ru–O–Ru bond angles and shorter Ru–O bond lengths.[108] The reader is again informed that the electronegativities of Ho and Y according to the CRC Handbook of Chemistry and Physics are 1.23 and 1.22, respectively.[133] However, as with most trends, there are exceptions. Hubert *et al.* reported that $Bi_2Ru_2O_7$ showed significantly lower OER activity than $Y_2Ru_2O_7$, $Nd_2Ru_2O_7$, and $Gd_2Ru_2O_7$, despite Bis electronegativity (2.02) being closer to that of Ru (2.2) than the others.[99]

3.2 Activity trends are subject to change

An important consideration is that electrocatalyst activity trends evolve with testing time.[99] Bulk properties alone cannot explain performance, as the interfacial environment in aqueous media plays a critical role.[104] During potential cycling, pyrochlores undergo surface reconstruction, which alters activity.[104]

Iwakura *et al.* found that film-type $Bi_2Ru_2O_7$ benefits from preconditioning, unlike its pellet counterpart.[81] The enhanced OER activity following KOH pretreatment was attributed to the formation of higher valence Ru species rather than increased surface area. However, this improvement was not observed in acidic electrolyte (0.5 M H_2SO_4).[81]

Initial high currents may also arise from catalyst dissolution and surface reconstruction.[99] Hubert *et al.* reported A-site and Ru dissolution across all $A_2Ru_2O_7$ pyrochlores investigated.[99] Indeed, in many cases, the OER activity of Ru- and Ir-based pyrochlores is linked to the leaching of A-site cations, which yields more active (often amorphous) BO_x surface structures.[89,106] These reconstructed surfaces can also become more stable over time.[106] Further discussion is provided in Section 5.3.

3.3 Stuffed pyrochlores

Stuffed pyrochlores involve B-site substitution without the use of foreign dopants. The earliest pyrochlores reported for OER applications were of this type.[4,64,65] Examples include $Pb_2(Ru_{2-x}Pb_x)O_{6.5}$[71] and $Y_2(Ru_{1-x}Y_x)O_{7-x/2}$,[77,91] which frequently display enhanced OER activity relative to their stoichiometric counterparts. This improvement may be attributed to increased surface area[71,91] and, in cases like $Y_2(Ru_{1.6}Y_{0.4})O_{6.8}$,

the introduction of Ru^{4+}/Ru^{5+} mixed valence states.[91] Interestingly, the A-cation can sometimes occupy B-site positions unintentionally. Park *et al.* used stoichiometric Y and Ru to synthesise $Y_2Ru_2O_7$ but obtained $Y_2(Ru_{2-x}Y_x)O_7$.[77] Similarly, Kim *et al.* used stoichiometric Y:Ru with a porogen and obtained both $Y_2Ru_2O_7$ and the stuffed variant $Y_2(Ru_{1.6}Y_{0.4})O_7$.[91] Both studies observed an increase in Ru oxidation state, and Kim *et al.* reported a structure rich in oxygen vacancies.[77,91] Lead-stuffed pyrochlores also exhibit high oxygen vacancy concentrations and strong OER performance.[65,114] The lattice parameter is typically increased in stuffed structures.[72] However, no consensus exists on an optimal A-site substitution level. Horowitz *et al.* found surface area variation to be composition-dependent, thus affecting activity unpredictably.[4] In contrast, Parrondo *et al.* observed a decline in OER activity when the Ru content at the B-site decreased.[72] Additionally, synthesis temperature can influence the degree of A-cation substitution into the B-site.[114]

3.4 Doping in the A-site

Doping is widely used to tune the electronic structure of pyrochlores without replacing the entire A- or B-site. A-site doping is the most common strategy, and the first study linking A-site doping to the OER activity of pyrochlores appeared in 2019 (Zn-doped),[67] although Lebedev *et al.* previously employed mixed A-sites (Bi/Y).[89] A broad range of A-site dopants including alkali-, alkaline earth-, transition-, basic-, rare earth- and non-metals. Most studies use A-site acceptor dopants (lower valence than the host cation),[29,62,67,68,97,107,116,122,123] with some cases of isovalent doping.[76,89] Acceptor doping introduces defects to maintain charge neutrality. This involves oxidation of the B-site cation and/or formation of oxygen vacancies. As shown in Brouwer diagrams, the point of integer valence ($[e'] = [h^{\bullet}]$) shifts to lower oxygen pressures, pO_2 (cation is more easily oxidised), and the point of integer structure ($[V''_M] = [V^{\bullet\bullet}_O]$) moves to higher pO_2 since oxygen vacancies are more easily formed and a higher oxygen pressure is required to fill them.[134] Multiple studies confirm that A-site doping increases Ru valence and oxygen vacancies, which both enhance OER activity.[67,68,97,116]

Some exceptions exist: Shang *et al.* observed reduced Ru valence post-doping,[123] while others found only Ru oxidation and no oxygen vacancy formation,[29,107] or only oxygen vacancies and no valence state change.[62] The latter maintained unchanged Ru valence by using low dopant concentrations (10%), though other studies reported oxidation even at 7.5%.[67,68] This suggests that controlling dopant concentration can modulate the charge compensation mechanism. Regardless, most studies report enhanced Ru–O or Ir–O covalency following acceptor doping.[29,62,76,107,116,122,123]

Kuznetsov *et al.* observed that oxygen vacancy concentration increases with less negative formation enthalpy of the dopants binary oxide (weaker M–O bonds), facilitating lattice oxygen removal.[62] They also found stronger Ru–O covalency with less electronegative, more ionic dopants due to inductive effects.[62]

Table 4 The effect of A-site dopants in $Y_2Ru_2O_7$ pyrochlores on their OER activity

Dopant	Amount (%)	Ionic radius (Å)	BET ($m^2\ g^{-1}$)	Overpotential (mV at 10 mA cm^{-2})	Tafel slope (mV dec^{-1})
Pb[122]	20	1.29	18.8	195	45
Sr[29]	15	1.26	5.0	264	45
Ca[97]	12.5	1.12	7.9	275	40
Co[116]	12.5	0.9	—	275	61
Ba[68]	7.5	1.42	16.4	278	41
Zn[67]	7.5	0.9	4.2	290	37
Cu[62]	10	0.73	7.9	360	52

Table 4 summarizes OER performance for several A-site-doped $Y_2Ru_2O_7$ pyrochlores synthesised *via* sol–gel and tested in 0.5 M H_2SO_4. Surface areas range from 4.2 to 18.8 $m^2\ g^{-1}$.

A clear correlation is observed between A-site dopant radius and OER activity: activity increases with dopant size up to a point, then declines (*e.g.*, Ba). A similar volcano-type relation may exist with dopant concentration, constrained by solubility and lattice diffusion. The correlation between dopant size and amount of dopant is reasonable since larger dopants expand the lattice,[126] easing incorporation and allowing higher substitution levels without phase segregation.

Both larger A-site dopants and a higher concentration of these acceptor dopants can increase the oxygen vacancy concentration. Thus, enhanced activity may stem from increased oxygen vacancies (providing more active sites[135]) and electronic structure tuning. DFT studies show that acceptor doping shifts the metal d-band center upward (narrowing the d–p gap), improving both OER and ORR activity.[136] Oxygen vacancies also enhance Ru 4d–O 2p overlap[62] and raise the O 2p band toward E_F, increasing the DOS around E_F.[96] Strain effects may also contribute to activity: lattice expansion shifts metal d-states upward, increasing surface reactivity and modulating intermediate binding *via* d-state alignment with E_F.[137]

Activity declines at high dopant radius/concentration could reflect a critical vacancy threshold beyond which structural degradation occurs, forming ABO_3 or BO_2 phases.[5,96] Additionally, caution must be exercised when assigning dopant positions (A-site *vs.* B-site), as their precise location can be difficult to determine, even with structural refinements.[138] Therefore, especially at higher dopant concentrations, incorporation may occur at both the A- and B-sites, altering the perceived activity. It should also be noted that some studies report no vacancy formation upon doping.[29,107,139]

3.5 Changing or doping the B-site cation

B-site doping is primarily employed to reduce Ru content while tuning electrocatalytic properties. It was investigated for pyrochlore electrocatalysts more than two decades before A-site doping, with Prakash *et al.* doping Ru into an iridate pyrochlore.[71] Several other studies have explored mixed Ir–Ru B-sites.[69,87,101,110,112] This combination is particularly compelling due to reported synergistic effects between Ru and Ir.[87,101,140–142] Pittkowski *et al.* even suggested that Ru–Ir

synergy can suppress A-site effects.[101] However, some studies find no cooperative improvement in OER activity.[69,71] Prakash *et al.* did observe enhanced stability upon Ir doping.[71]

Studies reporting improved performance typically find an optimal dopant concentration near 50% ± 10%. This is feasible due to the similar ionic radii of Ru and Ir, enabling continuous solid solutions.[71] Pittkowski *et al.* identified peak performance at 45–55% Ru content, supported by DFT predictions.[101] Liu *et al.* reported peak activity at 40% Ir, with a decline at 50%.[110] Similarly, Matsumoto *et al.* found optimal OER activity at 50% Ir content.[112]

Pittkowski *et al.* linked activity to shorter Ru–Ir bond distances,[101] while Matsumoto *et al.* attributed performance gains to strengthened interactions between RuO_6 and IrO_6 octahedra *via* shared oxygen atoms.[112] Some studies noted a decrease in average Ru/Ir valence, linked to enhanced stability,[110,112] while others found valence to be composition-independent[101] or increased (though this may have resulted from A-site doping).[69] DFT simulations showed that the synergistic effect of Ru and Ir alters the d-band center, accelerating the potential-limiting step involving oxyhydroxide formation.[110] They also reported a widened gap between the O 2p band center and E_F, suppressing the lattice oxygen mechanism (LOM) and promoting stability.[110]

Isovalent B-site doping has also been explored using Ti.[115] Acceptor dopants, including Co,[94] Fe, Mn,[103,109,117] Mg, Ca, Sr,[127] and Pd,[129] have also been extensively studied. Some of these dopants have also been used in the A-site (Section 3.4). Dopant site assignment is usually governed by precursor ratios, suggesting many of these elements are soluble on both sites. However, solubility is generally lower for B-site doping: for example, Sr substitution is often limited to 5%,[127] whereas A-site doping permits up to 15%.[29] A 5% limit appears common for divalent B-site dopants.[103,129] Dopants with similar charge or radius to Ru can be incorporated in larger amounts.[71,109,115] However, as mentioned, caution should be exercised when definitively assigning site occupation as stoichiometry alone cannot determine whether a dopant resides on the A- or B-site without comprehensive structural analysis.[138]

Acceptor B-site doping requires charge compensation. Han *et al.* and Lee *et al.* observed both oxygen vacancies and Ru^{4+}/Ru^{5+} mixed valence in Mn-, Fe-, and Pd-doped $Y_2Ru_2O_7$.[103,129] Other studies report only Ru oxidation,[109] or no changes.[127] In these cases, stronger B–O covalency is commonly cited as a key factor for enhanced activity.[115,117,127] For example, Zhang *et al.* found $Y_2Ru_{1.9}Sr_{0.1}O_7$ to show improved performance, attributed to lattice distortion and greater metal–oxygen hybridization.[127] As with A-site doping, it is shown that distortion/strain can alter the relative positions of d- and p-bands leading to improved OER performance. Beyond Ru, Parrondo *et al.* showed that B-cations with more d-electrons or those from period 6 exhibited reduced OER activity.[72]

3.6 Modifying the O′ site/anion doping

The highly tunable structure of the pyrochlore also accommodates anion doping. Both S and F have been used, where S is less electronegative (2.58) than O (3.44), and F more (3.98). Consequently, M–S bonds are less ionic than M–O, while M–F bonds are more ionic. Wang *et al.* found that oxygen vacancy concentration in $Y_2Ru_2O_7$ increased with F-doping, attributed to the lower valence electron density of oxygen surrounding F, and thus weaker M–O bonds.[79] They further report that oxygen vacancy formation promotes LOM.[79] S-doping was also reported to increase oxygen vacancies in $Y_2Ru_2O_7$, though only up to a certain concentration.[128] However, the oxygen vacancy content was not directly measured, but instead inferred from increased surface-adsorbed oxygen. Additionally, S-doping induced an upshift of the Ru d-band toward E_F, which was said to strengthen the binding of oxygen intermediates and facilitate OOH* formation. A reduction in Ru valence was observed in both cases (F- and S-doped).[79,128]

4 Methods to detect oxygen vacancies

As discussed, oxygen vacancies play a key role in enhancing the OER activity of pyrochlores. Therefore, accurate methods for quantifying their concentration are invaluable, and these are summarised in Table 5. XPS has been the most used tool to determine the presence of oxygen vacancies, though interpretations of the spectra vary. For example, Gayen *et al.* deconvoluted the O 1s spectrum of $Pb_2Ru_2O_{7-\delta}$ into peaks at ∼528.4 eV (lattice oxygen), ∼530.15 eV (oxygen vacancies), and ∼531.1 eV (hydroxyl).[95] In contrast, Liu *et al.* assigned peaks at 529.3 eV (lattice O), 530.5 eV (hydroxyl), 531.9 eV (defective O), and 533.3 eV (adsorbed O).[102] Yan *et al.* provided similar assignments.[108] Feng *et al.* used only two peaks (529.3 and 531.4 eV), attributed to lattice and adsorbed oxygen, respectively.[67] They found decreased lattice O and increased adsorbed O upon Zn doping. Kuznetsov *et al.* observed surface oxygen vacancy signals at 531 eV, with other peaks at 529.5, 532, and 533.5 eV assigned to lattice oxygen, surface species, and adventitious oxygen.[62] Other studies assign the 530.9 eV peak to oxygen vacancies, with nearby peaks representing lattice oxygen and hydroxyls.[129] Wang *et al.* split the spectrum into four peaks (529.5, 531, 532, 533.5 eV), while Yang *et al.* used only two: 528.68 eV (lattice) and 531.18 eV (adsorbed). They suggested that oxygen vacancies correlate with adsorbed oxygen.[79,128] Table 6 summarises the O 1s XPS peak assignments in pyrochlores found in the literature.

5 Electrochemical testing of pyrochlore activity and stability

Now that we have examined the various factors affecting the electrochemical performance of pyrochlores, it is necessary to consider how activity changes are evaluated. In Tables 1–3, activity is expressed as the overpotential at 10 mA cm^{-2} (geometric), following common procedure in literature. However, due to variations in surface area arising from differences in synthesis methods and catalyst compositions, a meaningful comparison should rely on the actual electrochemically active

Table 5 Summary of characterisation techniques for oxygen vacancies in pyrochlores

Technique	Information obtained	Ref.
Photoluminescence (PL)	Emission intensity (*e.g.*, 400 nm) correlated to V_O	129
Iodometry	Quantitative measurement of V_O	118
Normalized electron spin resonance (ESR)/electron paramagnetic resonance (EPR)	Detection of oxygen vacancy signals (g = 2.002); qualitative/semi-quantitative analysis	29, 78 and 116
Temp.-programmed reduction (TPR, 700 °C, H_2 atmosphere)	Total oxygen content inferred from evolved water (detected with moisture meter) during reduction	88
Thermogravimetric analysis (TGA)	Oxygen release tracked *via* sample mass loss under varying atmospheres; can be coupled with MS for composition analysis	75 and 103
XANES	Probes oxidation states and indirectly reveals oxygen non-stoichiometry	91
Neutron diffraction	Structural resolution of oxygen site occupancy	139
Hall measurements	Carrier concentration correlates with oxygen vacancy-induced free electrons	78
XPS (O 1s spectra)	Surface defect states; interpretation varies depending on fitting and assignments	62, 67, 79, 95, 102, 108, 128 and 129
Raman spectroscopy	Intensity changes (*e.g.*, 700 cm^{-1} peak) associated with [V_O]	119

Table 6 O 1s XPS peak assignments in pyrochlores, grouped by binding energy

Binding energy (eV)	Assigned species	Ref.
~528.4–529.5	Lattice oxygen (M–O bonds)	62, 67, 79, 95, 102, 108, 128 and 129
530.15–531.0	Oxygen vacancies or near-vacancy lattice oxygen	62, 79, 95 and 129
530.5–531.4	Hydroxyl or adsorbed oxygen species	67, 79, 102, 128 and 129
531.9–533.5	Surface oxygen, adventitious species	62, 79, 102 and 108

surface area (ECSA) rather than the geometric one. Furthermore, a current density of 10 mA cm^{-2} is not representative of industrial electrolysis conditions, which typically require current densities above 100 mA cm^{-2} (1 kA m^{-2}). Therefore, a reliable method of extrapolation, such as Tafel slope analysis, is needed to predict performance under realistic conditions.

In some studies, carbon was incorporated as a conductive additive to improve pyrochlore conductivity,[20,67,68,97,99] while others used inks without added carbon.[62,75,101,102] This makes it especially important to use intrinsic, rather than extrinsic, metrics when comparing catalyst activity. Conductivity in the catalyst layer influences the ECSA, thereby affecting performance. Although surface area measured by BET can be informative, it may not fully represent the electroactive surface. Conductive additives may activate previously inaccessible regions of the catalyst by overcoming conductivity limitations.

Given the challenges of reliable area normalization, ranking catalysts based on intensive quantities is preferable. One example is the adsorption energy of key intermediates. Recent studies show that such energies can be integrated into microkinetic models and extracted through fitting to polarization curves.[143,144]

The literature often treats Tafel slope as a proxy for catalytic activity, implying that lower slopes indicate more active catalysts.[20,97] However, this assumption lacks robust support, especially given variations in testing conditions. For example, the same catalyst can exhibit drastically different behaviour in different electrolytes.[145] Oversimplified polarization curve analyses can misrepresent the electrocatalytic mechanism.[48] Tafel slopes are traditionally used to evaluate kinetics and deduce the rate-determining step, often based on the assumption of either full or negligible adsorbate coverage. Yet, in practice, Tafel slopes are often influenced by variable coverage, making such assumptions invalid.[48]

For many proposed mechanisms, more than one linear region may be expected in the polarization curve, as shown in classic studies by Bockris and co-workers.[43,44] Moreover, in catalysis research, significant current can be observed even at low overpotentials. Not all mechanisms exhibit classic Tafel behaviour.[146] As such, direct fitting of polarization curves to microkinetic models represents a more rigorous alternative.[143,144,146,147]

5.1 Surface area determination and normalisation

As discussed in the preceeding section, normalising the activity of OER electrocatalysts is essential for meaningful comparison. Normalisation with respect to ECSA is one of the most accurate approaches. Numerous studies on pyrochlore electrocatalysts report ECSA values obtained from double-layer capacitance measurements.[116,117,119] However, no standardised protocol exists across all OER electrocatalysts.

Watzele and Bandarenka proposed a fast and facile method to determine the ECSA of electronically conducting oxides and perovskites,[148] which could be well suited for pyrochlores. Their method leverages specifically adsorbed OER intermediates (at low overpotentials) to determine the adsorption capacitance, C_a, analogous to approaches used in CO adsorption or hydrogen underpotential deposition. Electrochemical

impedance spectroscopy (EIS) is used to extract C_a, which is assumed to be related to the surface coverage of adsorbates through

$$C_a = -q_a\left(\frac{d\theta_a}{dE}\right) \quad (33)$$

wherein θ_a is the adsorbate fractional coverage and q_a is the charge required to form an adsorbate layer.[148] Eqn (33) defines a steady-state pseudocapacitance, which does not, in general, coincide with the adsorption *ac* pseudocapacitance determined from impedance measurements. (for a discussion, see ref. 149). However, the capacitance determined by impedance is expected to be proportional to the surface area, and the method can still work if calibration samples are available. Alternatively, some studies have used integration of the Ru^{4+}/Ru^{6+} redox peaks for normalization,[126] *cf.* also ref. 150.

5.2 The importance of cyclic voltammetry

Cyclic voltammetry (CV) is a facile electrochemical technique that provides mechanistic insight into redox behaviour. Goodenough *et al.* reported three redox peaks for $Pb_2Ru_2O_7$ at 0.1, 0.9, and 1.1 V *vs.* SCE, assigned to Ru^{2+}/Ru^{3+}, Ru^{3+}/Ru^{4+}, and Ru^{4+}/Ru^{5+}, respectively.[64] In alkaline media, the Ru^{2+}/Ru^{3+} peak was suppressed, while the other two were shifted negatively (by $\sim$60 mV per pH).[64] Gokagac and Kennedy observed two peaks for $Bi_2Ru_2O_7$ at 0.0 and 0.45 V *vs.* MMSE, ascribed to Ru^{3+}/Ru^{4+} and Ru^{4+}/Ru^{5+}.[84]

While some publications do not mention A-site redox transitions, others do. Prakash *et al.* observed an increasing anodic current with superimposed small peaks and a broad cathodic peak.[70] These features were attributed to successive surface Ru oxidation events and possible Pb oxidation. Ten Kortenaar *et al.* clearly identified A-site redox features in CVs of several iridate pyrochlores.[65] In $Pb_2(Pb_xIr_{2-x})O_{7-y}$, a small capacitive background and several quasi-reversible peaks were observed, including a doublet between -1.1 and -0.85 V *vs.* SSE, attributed to Ir^{3+}/Ir^{4+} and an unidentified process (only visible under Ar). Peaks at -0.33 V and -0.13 V *vs.* SSE were assigned to Ir^{4+}/Ir^{5+} and Pb^{2+}/Pb^{4+}. In $Eu_2Ir_2O_7$, similar transitions (Eu^{2+}/Eu^{3+}) were proposed but less pronounced. $Bi_2Ir_2O_7$ also showed a distinct doublet with Ir^{4+}/Ir^{5+} shifted positively. CVs for Bi- and Nd-based pyrochlores yielded irreversible cathodic peaks or none at all, correlating with reduced OER activity and suggesting that A-site redox activity may enhance performance.[65]

Prakash *et al.* noted that CV features depend heavily on cycling history and synthesis conditions, complicating interpretation.[71] While the observed charge is likely due to multiple Ru redox transitions, the sweep-rate dependence was minimal—unlike typical RuO_2 behaviour. In a recent study, CVs of $Tb_2Ru_2O_7$ (and related pyrochlores) displayed two peaks at 0.7 and 1.1 V *vs.* RHE, assigned to Ru^{3+}/Ru^{4+} and Ru^{4+}/Ru^{6+} transitions.[126] Notably, overoxidation to Ru^{8+} (as seen in RuO_2 and $SrRuO_3$ at $\sim$1.35 V) was not observed in the pyrochlore, indicating enhanced stability.[126]

5.3 Stability

Instability of oxide electrocatalysts during the OER typically manifests through lattice oxygen participation in evolved O_2, cation dissolution, or structural/compositional changes.[151] Stability can be defined in various ways for electrocatalysts in aqueous media. Grimaud *et al.* define bulk oxide stability as the absence of significant metal ion or structural integrity loss during the OER as detected by TEM or spectroscopy.[61] This definition differs from thermodynamic stability discussed by Binninger *et al.*, which is related to Pourbaix diagrams.[61,151]

Most studies prioritise electrocatalyst activity over long-term stability,[152,153] yet the latter is crucial for large-scale applications, particularly in PEM water electrolysis (PEMWE). Chen *et al.* demonstrated that a catalyst with lower activity but higher stability can cut energy costs by 43% after 2000 hours of operation.[153] Interestingly, activity and stability are often inversely correlated.[60,152–154]

Several comprehensive reviews outline OER electrocatalyst stability, including the mechanisms of degradation/deactivation, figures of merit, strategies to improve the stability and how to effectively analyse stability.[152–155] Spori *et al.* categorise stability into material stability (*e.g.*, Pourbaix and mechanical stability, crystallinity) and operational stability (*e.g.*, support passivation, dissolution, particle growth).[152] Feng *et al.* provides a review on the degradation of the entire PEMWE system.[156]

Pourbaix diagrams are an established tool for assessing thermodynamic stability at specific pH and potential. However, as electrochemical systems often operate far from thermodynamic equilibrium, these diagrams are not always predictive of observed stability.[157] They can be useful as a predictive and interpretative tools,[153,157] though other factors—such as transient dissolution, metastable phases, strain, and interfacial effects should be considered.[157]

Stability enhancement strategies include doping/alloying, morphological tuning, and support selection.[152] This section addresses these aspects, the mechanisms underlying electrocatalyst degradation, key evaluation considerations, and specific insights into pyrochlore behaviour.

5.3.1 Interfacial electrochemical reaction. The electrode–electrolyte interfacial reaction strongly influences stability.[157] As discussed in Section 2, the OER mechanism might determine degradation pathways.[153] LOM may compromise stability due to lattice oxygen involvement. As outlined in Section 2.3, it leads to lower Tafel slopes and greater dissolution due to stress on the oxide layer through restructuring.[153,158] Ru has been shown to follow LOM, but Pt and Pd, believed to follow AEM, show higher Tafel slopes and less dissolution.[153] This supports the frequently observed activity-stability trade-off, though the correlation is still debated.[153]

Whether an electrocatalyst follows LOM depends on composition, structure, defects, and crystallinity.[153] OER at RuO_2 is usually believed to proceed through LOM, but Stoerzinger *et al.* showed that it is not observed on crystalline RuO_2 surfaces that are still very active.[159] This challenges the belief that activity and stability are unequivocally linked, and shows that tuning factors like crystallinity could optimise both.[153]

LOM does not necessarily equate instability since the oxides can reach a metastable state. Instead of dissolving, the metal ion recombines with hydroxide anions and returns to its initial state, closing the cycle. Thus stability is possible if recombination is favoured over dissolution. This can be engineered by reducing the oxygen mobility or replacing oxygen with an anion that is less easily oxidised.[151,152] The structure can also be tuned so that coordinate structures under the surface layer stabilise the lattice oxygen.[153]

Rong *et al.* discuss a third mechanism, the oxide path mechanism (OPM), in which only O_{ad} and OH_{ad} act as intermediates, allowing direct O–O coupling without oxygen vacancy formation.[155,160] Lattice oxygen is not involved, and the mechanism requires specific configurations of active sites.[155]

Pyrochlores are commonly engineered with oxygen vacancies to favour LOM.[62,91,114] Excessive vacancies can compromise stability through amorphisation and dissolution.[60] Adjusting the A-site to upshift the O 2p band center enhances metal–oxygen hybridization and promotes the AEM-to-LOM transition.[104] Conversely, lowering the O 2p band center can improve stability by circumventing LOM.[110] In another example, fluoride doping of $(Ir_{0.3}Sn_{0.3}Nb_{0.3})O_2$ was used to shift the d-band center downward, mimicking the electronic structure of IrO_2, thereby increasing activity while maintaining stability.[161] These cases demonstrate that modifying the electronic structure can be an effective strategy to tune both OER activity and stability, and that these factors are not always linked.

5.3.2 Dissolution and surface reconstruction. Dissolution and the OER are likely linked by a common intermediate.[152] All non-noble metals have high dissolution rates in acidic media, necessitating the use of noble metal OER electrocatalysts. Moreover, catalysts can also be consumed through organic impurities that chelate or complex metal ions.[152]

Dissolution can be categorised as chemical, electrochemical and transient.[154] Chen *et al.* classifies dissolution as transient and steady-state (constant potential).[153] Chemical dissolution occurs through interactions between electrocatalysts and components or impurities in the electrolyte/electrolyser, such as acid–base reactions with protons that destabilise first-row transition metal oxides.[154] However, it is not only these metals that are subject to chemical dissolution. Zeng *et al.* summarise multiple studies where the chemical dissolution of Ir has been observed from mixed oxides.[154]

Electrochemical dissolution is subject to an applied potential forming unstable species and can be reductive or oxidative.[154] The latter is most prominent in OER electrocatalysts. Potentials applied during the OER lead to the formation of unstable species, like volatile RuO_4 that forms when RuO_2 is subjected to potentials above 1.4 V according to the eqn (34):[152,154]

$$RuO_2 + 2H_2O \rightarrow RuO_4 + 4H^+ + 4e^- \quad (34)$$

OER and dissolution both take place through the formation of RuO_4 as a common intermediate and it is the stability of another intermediate $(RuO_2(OH)_2)$ that determines if RuO_4 corrodes or produces O_2 and $RuO_2(OH)_2$.[162] Ir incorporation into RuO_2 increased the stability by reducing Ru dissolution, but the inherent Ir stability was decreased.[142] Distinct oxidative dissolution mechanisms, which are not yet fully understood, can be observed when different facets, substrates or reaction potentials are considered.[153] In some cases, such as shut-down or start-up of electrolyser systems, reductive dissolution might also be relevant.[154]

Transient dissolution occurs under potentiodynamic polarisation, where local pH changes and phase transitions are apparent.[157] Fluctuating potential disrupts the crystal structure *via* oxidation/reduction, during which oxygen atoms are inserted or removed and/or metastable phases form.[154] These phases are difficult to characterise and may enhance activity at the cost of stability.[157] Transient dissolution for Ir and Ru electrocatalysts take place *via* oxidation/reduction of RuO_2 and reduction of Ir to unstable metallic complexes.[154]

Chen *et al.* define transient dissolution as surface restructuring prior to steady-state dissolution. For Ru, steady-state dissolution dominates, while transient dissolution is more pronounced for Ir and Pt.[153,158] Notably, transient dissolution of Ru-based catalysts have occurred below the OER onset, implying surface redox reactions also contribute to instability.[153] Furthermore, oxidative (anodic) and reductive (cathodic) transient dissolution correlate with M–M and M–O bond strength, respectively.[157] Since transient dissolution arises during oxidation to oxides/(oxy)hydroxides, directly preparing these phases can reduce its extent.[153] Strain also plays a critical role: oxidation/reduction and intermediate adsorption induce local lattice strain, altering the lattice constant and electronic structure, thereby influencing stability.[157] When potential shifts outpace structural relaxation, strain can accumulate and exacerbate degradation.[157]

Dissolved species may redeposit *via* three pathways: phase segregation, active-phase reconstruction, and dynamically stable active sites.[153] The first generally reduces activity, while the latter two enhance it. Active-phase reconstruction, typically a dissolution–redeposition process, can also be tuned *via* dopants or temperature.[153] Particle growth may also result from redeposition, though Ostwald ripening and coalescence also contribute.[152] Redeposition depends on operating potential and ion concentration, and balancing dissolution and redeposition rates can lead to dynamic stability.[153] However, in circulating electrolytes (*e.g.*, full cells), ions are flushed out, limiting redeposition, unlike in 3-electrode setups.[152,153] This highlights the difference between full- and half-cell testing. Moreover, isotope labelling used to confirm LOM, might detect dissolution–redeposition pathways instead.[153]

Dissolution of active and inactive ions, along with surface restructuring, is widely reported for pyrochlores. Prakash *et al.* linked OER degradation in lead ruthenates to Ru and Pb loss, attributed to low crystallinity and residual RuO_2 and PbO phases.[71] Applying a conductive ionomer overlayer mitigated dissolution.[71] Lebedev observed Y leaching from a pyrochlore, forming active IrO_2 on the surface.[89] Similarly, A-site cation loss (*e.g.*, Ca and Na) has been reported without compromising

structure or activity since charge neutrality was maintained *via* proton incorporation as bridging hydroxyls.[69] Galyamin *et al.* detected surface reconstruction in R_2MnRuO_7 (R = Y, Tb, Dy) pyrochlores through hysteresis in initial voltammograms that diminished with continued cycling, accompanied by rising OER activity.[117] Hubert *et al.* concluded that all pyrochlores studied were thermodynamically unstable under OER conditions, and reported varied stabilities across studies.[99] They ascribe this to non-standardised methods to assess stability and emphasise the need to measure dissolution in parallel with OER activity.[99]

5.3.3 Choice of support. Electrocatalysts for the OER are often supported to enhance conductivity, increase surface area, and reduce noble metal loading. As such, the effect of the support material on stability must be considered. Under oxidising conditions, carbon-based supports can become passivated, leading to apparent performance degradation.[152,163] Support oxidation may also cause particle detachment.[152] For example, Geiger *et al.* caution against using glassy carbon as a backing electrode for stability testing in three-electrode cells due to oxidation and passivation.[163] This process creates a feedback loop: oxide growth reduces conductive area, increasing the current density at remaining sites, which accelerates passivation until full deactivation occurs.[154]

The interaction between catalyst and support, ranging from weak electrostatic forces to strong chemical bonds, influences catalyst adhesion and stability.[152] These interactions also modify electron density and impact activity. Strong support-catalyst binding may lower the metal oxidation state *via* charge donation, thereby suppressing metal dissolution during OER.[152,164] A study on IrO_x found that supported nanocatalysts were more active but less stable, where carbon proved to be the least stable support and annealing unsupported IrO_x offered a better balance between stability and activity.[165]

How the catalyst is adhered to the support is important, and methods include binders and co-crystallisation.[152,166] For pyrochlores, carbon-based supports are predominantly employed. Glassy carbon (GC) rotating disk electrodes (RDEs) are commonly used in three-electrode configurations,[62,101,102] often in conjunction with additives like acetylene black,[67,68,97] activated carbon,[120,121] carbon black,[116,118] or Vulcan 72.[37,122] Carbon paper[87] and rotating ring-disk electrodes (RRDEs) with a GC disk and Pt ring are also used.[100] RRDEs allow concurrent monitoring of OER activity and catalyst dissolution.

5.3.4 Surface blocking. The active area, electrode morphology, composition of catalyst layer, electrolyte species and testing conditions can affect bubble detachment, which will affect activity and stability.[152] Gas bubbles can block surface sites, which will lead to an apparent decrease in the observed performance. In three-electrode testing, micro-bubbles that cannot be completely removed is an experimental artifact that can affect the observed stability.[153]

Certain anions will have a stronger interaction with the catalytic sites and could significantly impact the performance as shown by Owe *et al.*[145] (*e.g.* use of $HClO_4$ compared to H_3PO_4) Furthermore, impure electrolytes containing small amounts of metal cations such as Mn, Pb and Co could lead to simultaneous formation of oxides at catalytic sites.[167] Dissolved cations can also block conductive H^+-sites in the ionomer.[69]

5.3.5 Probing stability. Most studies assess electrocatalyst stability by applying a constant current and observing potential changes, or by applying a constant potential and monitoring current decay. Spöri *et al.* report that most stability tests are conducted at 80 °C and 1–2 A cm^{-2} for 24–100 hours.[152] However, decreased activity is not the only sign of degradation. Dissolution or leaching can increase surface area or expose more active layers, masking instability.[152,163] Unspecified loading can further obscure true performance since inner layers can become available as the material degrades.[163] Larger surface areas may also accelerate degradation under constant potential. Thus, measurement duration and methodology are critical for stability assessment.

A decline in activity may result from various mechanisms: passivation, detachment, dissolution, surface blocking, or agglomeration, each with different implications.[163] Complementary techniques such as CV and EIS should be used, but Spöri *et al.* found that only a third of PEM studies included such analyses.[152] EIS provides insights into ohmic resistance (R_s) and charge transfer resistance (R_{ct}), which can indicate passivation or structural changes, respectively.[154]

There is currently no standardised protocol to probe deactivation mechanisms. Thorough pre- and post-characterisation *via* techniques such as XRF, XRD, SEM-EDX, (S)TEM, APT, Raman, and XPS is essential to track compositional and morphological changes.[152,153] Mass losses can be assessed using electrochemical quartz crystal microbalance (EQCM) or inductively coupled plasma mass spectrometry (ICP-MS). These enable calculation of the stability number (S-number), the ratio of evolved O_2 to dissolved active material.[168] The S-number is independent of catalyst loading and surface area, providing a meaningful measure of intrinsic stability.[153,154] Another useful metric is the activity-stability factor (ASF), which indicates the ratio between the OER- and dissolution current densities.[154]

Stability testing is most often done in half-cells. Chen *et al.* recommend long (hundreds of hours) CA or CP, combined with dissolution analysis, as the most reliable approach.[153] In a three-electrode cell, 10 mA cm^{-2} is a commonly accepted benchmark. The current density may be reported relative to the geometric or electrochemically active surface area, with the latter being more meaningful but harder to obtain.

Accelerated lifetime tests (ASTs) using CVs are widely applied, especially for ORR catalysts.[152] Chen *et al.* note that while extensive cycling reflects start-up/shut-down behaviour, it should not be the sole indicator of stability due to structural redox changes.[153] Zeng *et al.* describe a case where CA showed activity loss while CV suggested stability attributed to cathodic sweeps reversing anodic degradation.[154,169] Nonetheless, Spöri *et al.* suggest that selecting appropriate potential limits can prevent irreversible changes.[152] CV results depend on scan rate and potential range, complicating comparisons.[153] CP is also limited by fluctuating potentials that affect electrooxidative conditions depending on catalyst activity, unlike CA.[154] A combination of CA, CP, and CV is thus advisable.[154]

Stability testing of pyrochlores varies widely. Some studies combine cycling (*e.g.*, 1500 cycles at 100 mV s^{-1} from 1.4–1.6 V in 0.5 M H_2SO_4) with CP,[68,117] or CV (2000 cycles, 1.35–1.6 V) with CA at 1 mA cm^{-2} for 8.5 hours.[67] Others use only CP (1.5 V, 20 hours),[98] or only CA.[119] Several also combine galvanostatic holds with ICP-MS to quantify dissolved species.[62] Full-cell testing has also been employed.[67–69,97,117] Burnett *et al.* used mass spectrometry to directly monitor oxygen evolution.[69] This analysis would enable the use of the S-number.

A standardised OER stability protocol was proposed by Spöri *et al.*, applicable to both half- and full-cell testing.[152] The protocol begins with two potential cycles (from 1.23 V *vs.* RHE to the potential yielding 20 mA cm^{-2}), followed by redox and surface area analysis *via* CV (50 mV s^{-1}) and EIS. The first two cycles are then repeated before a series of CP steps from 0.1–20 mA cm^{-2} (10 minutes each) is performed, followed by galvanostatic stability testing at 20 mA cm^{-2} for 24 hours. These steps are repeated to assess changes after stability testing. These tests should be at 80 °C and 1600 rpm (for RDE), and full-cell tests should have a flow ratio of 3. In a full cell, galvanostatic testing at 1 A cm^{-2} for 24 hours is suggested for pre-screening (to compare with published results), followed by full validation at 2 A cm^{-2}.[152] Since real-life operation (20 000–50 000 hours) cannot be directly assessed, ASTs such as CV or square-wave voltammetry (0.05–1.4 V) are recommended.[152]

Fundamental differences exist between half-cell and full electrolyser testing. Variations in pH, applied potential, support materials, and ionomer content may alter surface reconstructions or introduce morphological/electronic differences.[153] The ionomer, acting as both binder and ionic conductor, must be carefully dosed since too much blocks active sites and impedes mass transfer, and too little increases resistance.[153]

6 Recommendations for testing activity and stability

6.1 Experimental procedures

For screening the electrocatalysts, we recommend performing 5–10 initial CV measurements in the non-OER region to observe how the electrocatalyst behaves and whether it changes upon preconditioning. After this, an LSV measurement should be performed to evaluate the OER activity. It is preferable to record the polarisation data across the widest possible range, up to at least 1.6 V. Especially if the data do not show any truly linear sections in the *E vs.* log *i* plots over at least a decade, it becomes important to have as wide a data range as possible for fitting to models (see below). Furthermore, we recommend the use of CVs at different scan rates (from 50–500 mV s^{-1}) in the non-faradaic region to determine the double layer capacitance. This can then be divided by a specific capacitance value of 0.35 mF cm^{-2} (ref. 170) to obtain ECSA, which we recommend to normalise the OER activity. This is used instead of the geometric area to enable comparisons across different labs.

6.2 Analysis

When plotting logarithmic current–potential curves for Tafel analysis, we recommend displaying the full current range. This enables fitting of a microkinetic model to the entire curve, rather than restricting the analysis to short linear regions for Tafel slope determination. Plotting deviations from the microkinetic model (or Tafel's equation if that is employed) to assess the quality of the model is generally recommended to highlight any systematic deviations between theory and experimental data.

Microkinetic models can be used to evaluate intensive parameters related to the adsorption of intermediates on the surface, providing information independent of testing conditions, loading, or catalyst surface area.[143] An overview of the reaction mechanisms was provided in Section 2.4. These mechanisms can be converted to mathematical expressions for current density, as detailed in works by Marshall *et al.*,[146,147] Shinagawa *et al.*,[48] Reksten *et al.*,[143] and Scott *et al.*[144] Many proposed reaction schemes can be fitted into the scheme proposed by Giordano *et al.*,[171] as a sequence of concerted or separate proton and electron transfers. Reksten *et al.*[143] derived a general expression for this scheme, allowing computation of any reaction pathway within it. For solid solutions of IrO_2 and RuO_2, the data fit well to eqn (35) (describing the CC mechanism outlined by Reksten *et al.*), both in terms of reaction order and current–potential behaviour.

$$i_{CC} = \frac{4FTk_2^0 \exp[(1-\alpha_2)F(E-E_0)/RT]}{1 + K_1 a_{H^+} \exp[-F(E-E_0)/RT]} \quad (35)$$

Fits to eqn (35) can be performed in terms of the pre-exponential factor in the numerator, the transfer coefficient α, and the constant K_1. The latter can be related to the energy of adsorption for oxygen through the scaling relations introduced in Section 2.4, as described by Reksten *et al.*[143]

$$K_1 = \exp\left\{\frac{0.61\Delta E_O - 0.55\ \text{eV} - eE^0}{6.242 \times 10^{18}\ \text{eV J}^{-1} \cdot k_B T}\right\} \quad (36)$$

in which ΔE_O is the binding energy for oxygen, k_B the Boltzmann constant, e the elementary charge and E^0 the standard electrode potential. Thus, the data may be fitted directly with the binding energy for oxygen as a fitting parameter.

However, owing to the scaling relations and hence the ratios between rate constants for the forward and reverse directions of the rate equations they dictate, equally good fits should be expected for a model assuming the third reaction step to be rds. We refer to this model as the CCC model in line with the reference, for which the current is given by

$$i_{CCC} = \frac{4FTk_2^0 \exp[(1-\alpha_2)F(E-E_0)/RT]}{1 + K_2 a_{H^+} \exp[-F(E-E_0)/RT] + K_1 K_2 a_{H^+}{}^2 \exp[-2F(E-E_0)/RT]} \quad (37)$$

As discussed in ref. 143, the scaling relations imply that $K_1 \ll K_2$, the last term in the denominator becomes negligible, and the equation attains the same form as eqn (35). In this case, K_2 becomes the relevant constant from which the binding

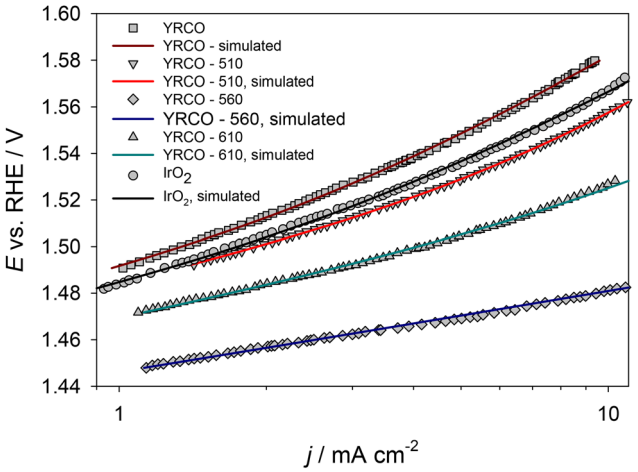

Fig. 16 The CCC equation[143] (eqn 37) fitted to values of electrode potential *vs.* logarithm of current density for YRCO, YRCO-X, and IrO_x from Kim *et al.* 2019.[94,143]

energy must be evaluated,[143]

$$K_2 = \frac{0.39\Delta E_O - 0.60\ \text{eV} - eE^0}{6.242 \times 10^{18}\ \text{eV J}^{-1} \cdot k_B T} \quad (38)$$

As an example of the application of this to pyrochlores, we fitted the curves reported by Kim *et al.* for $Y_2Ru_{2-x}Co_xO_7$ with both the CC, eqn (35), and CCC, eqn (37) mechanisms outlined by Reksten *et al.*[143] The fit to the eqn (37) is shown in Fig. 16. The polarization data reported by Kim *et al.* do not appear to display any straight sections and therefore elude a straightforward assignment of a Tafel slope.[94] However, fitting eqn (37) to the same data sets appears to by and large capture their shape to a much higher degree. Ideally, these fits should have been performed over a much wider range. The binding energy values obtained by the fits were approximately equal to 2.3 eV for all data sets: IrO_2 2.26 eV, YCRO 2.28 eV, YCRO-510 2.37 eV and YCRO-610 2.31 eV. In Section 2.4, we have shown that an oxygen binding energy of 2.3 eV corresponds to the third step being rate-determining, which is consistent with the CCC model used in this case. The corresponding fits to the CC model, eqn (35), also gave more or less similar binding energies ΔE_O, but now equal to 3.4 eV. In view of the rather high value for the latter model as compared to the theoretically computed values,[45] we tend to prefer the CCC model, eqn (37).

For the data provided in Fig. 16, we somewhat surprisingly found very similar values for the binding energy for all the data sets, *viz.* 2.3 eV. With some reservation concerning the accuracy of the model and the scaling relations employed, this is what would result if the catalysts were to differ only in the electrochemical surface area per geometric surface area and not in the intrinsic activity, *i.e.* activity per electrochemical surface area. In order to reach a more definitive conclusion, however, a wider range of currents would be necessary. This highlights the importance of (1) expanding the range of currents and potentials to the widest possible and (2) using more complete, multistep kinetic models in the interpretation.

We also note in passing that when scaling relations are introduced into microkinetic models as in eqn (36) and (38), the result is inconsistent with the data; with ΔE_O = 2.3 eV eqn (37) predicts a transition from a low Tafel slope of approximately 40 mV to a slope of 120 mV at an electrode potential of approximately 1.55 V, which happens also be the onset potential for the OER according to Fig. 6(b). In other words, according to the combination of microkinetics and the scaling relations, one should not observe slopes in the E *vs.* $\log i$ curves lower than 120 mV. We are not aware of any attempts to resolve this conflict.

To evaluate stability, we recommend LSV and ECSA measurements after different cycling regimes and potential holds to understand how the activity and active area changes. We recommend using a combination of cycling in the OER region and potential holds, since the electrocatalyst might behave differently when cycled compared to when it is kept at a single potential. Furthermore, we recommend cycling in a lower potential region (between 0.2–1.3 V) to evaluate if this regenerates the catalyst. Since pyrochlores have been shown to reorganise the surface structure under these conditions, cycling in a lower potential region could lead to regained activity. We recommend the use of ICP-MS after each test to correlate the dissolution of elements to the stability trends. We also recommend the use of physical characterisation techniques such as SEM-EDX, XRD, Raman spectroscopy and XPS before and after stability tests to see how the structure and composition changes with testing.

7 Conclusion

Pyrochlores are versatile and highly tunable structures, making them excellent candidates for addressing current materials challenges, particularly the development of active, durable, and cost-effective electrocatalysts for the OER. Their tendency to form oxygen vacancies and support mixed-valence B-site cations, especially when acceptor-doped, has improved their OER activity significantly. However, the precise mechanisms by which doping or structural modifications enhance OER activity remain unclear and varying information is available in the literature with contradicting conclusions. This is one of the largest challenges faced in the development of ruthenate pyrochlores as active and stable OER electrocatalysts. Standardised electrochemical testing protocols are needed to enable more accurate comparisons across studies. Preliminary analysis of the literature suggests that differences in activity of ruthenate pyrochlores are primarily linked to variations in the pre-exponential factor rather than binding energy. In addition to electrochemical testing, more rigorous physical and *in situ* characterisation techniques need to be employed when assessing newly prepared pyrochlore compositions to address discrepancies in activity trends. A deeper understanding of the mechanisms behind enhanced electrocatalytic activity is essential. These insights will support the rational design of pyrochlores with optimised activity and stability for OER

applications. Furthermore, we address the possible stability issues that ruthenate pyrochlores could face and highlight the need for thorough stability testing to verify the use of these materials in electrolyser systems. Should the stability of the ruthenate pyrochlores be insufficient, further development of iridate pyrochlores might be required.

Conflicts of interest

There are no conflicts to declare.

Data availability

The authors of this manuscript hereby declare that the data is available in the supplementary information (SI). An editable spreadsheet summarizing literature where ruthenate or iridate pyrochlores have been used as OER electrocatalysts is provided in the supplementary information. See DOI: **https://doi.org/10.1039/d5ma00696a**.

Acknowledgements

This work is funded by the Research Council of Norway, project number 325873.

References

1 H. Sun and W. Jung, *J. Mater. Chem. A*, 2021, **9**, 15506–15521.
2 A. Reksten, F. Moradi, F. Seland and S. Sunde, *ECS Trans.*, 2014, **58**, 39.
3 W. Zhu, X. Song, F. Liao, H. Huang, Q. Shao, K. Feng, Y. Zhou, M. Ma, J. Wu and H. Yang, *et al.*, *Nat. Commun.*, 2023, **14**, 5365.
4 H. Horowitz, J. Longo and H. Horowitz, *J. Electrochem. Soc.*, 1983, **130**, 1851.
5 P. Gayen, S. Saha and V. Ramani, *Acc. Chem. Res.*, 2022, **55**, 2191–2200.
6 M. Kim, J. Park, M. Kang, J. Y. Kim and S. W. Lee, *ACS Cent. Sci.*, 2020, **6**, 880–891.
7 J. Xu, R. Xi, X. Xu, Y. Zhang, X. Feng, X. Fang and X. Wang, *J. Rare Earths*, 2020, **38**, 840–849.
8 A. P. Anantharaman and H. P. Dasari, *Ceram. Int.*, 2021, **47**, 4367–4388.
9 C. N. R. Rao and J. Gopalakrishnan, *New directions in solid state chemistry*, Cambridge University Press, 1997.
10 A. Shlyakhtina and L. Shcherbakova, *Russ. J. Electrochem.*, 2012, **48**, 1–25.
11 F. Wöhler, *Ann. Phys.*, 1826, **83**, 417–428.
12 B. C. Chakoumakos, *J. Solid State Chem.*, 1984, **53**, 120–129.
13 K. Moreno, A. Fuentes, J. García-Barriocanal, C. León and J. Santamaría, *J. Solid State Chem.*, 2006, **179**, 323–330.
14 R. E. Carbonio, J. A. Alonso and J. Martinez, *J. Phys.: Condens. Matter*, 1999, **11**, 361.
15 B. Mandal and A. Tyagi, *BARC Newsl.*, 2010, **313**, 6–13.
16 K. A. Gschneidner, J.-C. G. Bunzli and V. K. Pecharsky, *Handbook on the physics and chemistry of rare earths*, Elsevier, 2005, vol. 34.
17 M. Subramanian, G. Aravamudan and G. S. Rao, *Prog. Solid State Chem.*, 1983, **15**, 55–143.
18 Z. Teng, L. Zhu, Y. Tan, S. Zeng, Y. Xia, Y. Wang and H. Zhang, *J. Eur. Ceram. Soc.*, 2020, **40**, 1639–1643.
19 P. Wilde and C. Catlow, *Solid State Ionics*, 1998, **112**, 173–183.
20 J. Kim, P.-C. Shih, K.-C. Tsao, Y.-T. Pan, X. Yin, C.-J. Sun and H. Yang, *J. Am. Chem. Soc.*, 2017, **139**, 12076–12083.
21 P. Cox, J. Goodenough, P. Tavener, D. Telles and R. Egdell, *J. Solid State Chem.*, 1986, **62**, 360–370.
22 M. L. Sanjuán, *Pyrochlore Ceramics*, 2022, pp. 95–159.
23 L. Minervini, R. W. Grimes and K. E. Sickafus, *J. Am. Ceram. Soc.*, 2000, **83**, 1873–1878.
24 A. F. Fuentes, S. M. Montemayor, M. Maczka, M. Lang, R. C. Ewing and U. Amador, *Inorg. Chem.*, 2018, **57**, 12093–12105.
25 I. K. Allah, A. Bekka, R. E. Dinnebier, M. Kameche, N. Laouedj, W. Touati, C. Alaoui, Z. E. A. Bouziani, S. Lellou and M. Karmaoui, *J. Solid State Chem.*, 2022, **312**, 123189.
26 M. Pokhrel, S. K. Gupta, K. Wahid and Y. Mao, *Inorg. Chem.*, 2019, **58**, 1241–1251.
27 R. A. McCauley, *J. Appl. Phys.*, 1980, **51**, 290–294.
28 R. J. Cava, *Dalton Trans.*, 2004, 2979–2987.
29 N. Zhang, C. Wang, J. Chen, C. Hu, J. Ma, X. Deng, B. Qiu, L. Cai, Y. Xiong and Y. Chai, *ACS Nano*, 2021, **15**, 8537–8548.
30 J. Hubbard, *Proc. R. Soc. London, Ser. A*, 1964, **277**, 237–259.
31 D. Oka, Y. Hirose, S. Nakao, T. Fukumura and T. Hasegawa, *Commun. Phys.*, 2021, **4**, 269.
32 P. Cox, R. Egdell, J. Goodenough, A. Hamnett and C. Naish, *J. Phys. C-Solid State Phys.*, 1983, **16**, 6221.
33 W. Y. Hsu, R. V. Kasowski, T. Miller and T.-C. Chiang, *Appl. Phys. Lett.*, 1988, **52**, 792–794.
34 R. Kanno, Y. Takeda, T. Yamamoto, Y. Kawamoto and O. Yamamoto, *J. Solid State Chem.*, 1993, **102**, 106–114.
35 N. Taira, M. Wakeshima and Y. Hinatsu, *J. Solid State Chem.*, 1999, **144**, 216–219.
36 B. Kennedy and T. Vogt, *J. Solid State Chem.*, 1996, **126**, 261–270.
37 T. Liu, H. Guo, Y. Chen, Z. Zhang and F. Wang, *Small*, 2023, **19**, 2206698.
38 P. Sabatier, *La catalyse en chimie organique*, C. Béranger, 1920, vol. 3.
39 R. Parsons, *Catal. Electrochem.*, 2011, 1–15.
40 D. Newns, *Phys. Rev.*, 1969, **178**, 1123–1135.
41 B. Hammer, *Top. Catal.*, 2006, **37**, 3–16.
42 T. E. Jones, D. Teschner and S. Piccinin, *Chem. Rev.*, 2024, **124**, 9136–9223.
43 J. O. Bockris, *J. Chem. Phys.*, 1956, **24**, 817–827.
44 A. Damjanovic, A. Dey and J. Bockris, *J. Electrochem. Soc.*, 1966, **113**, 739.
45 J. Rossmeisl, Z.-W. Qu, H. Zhu, G.-J. Kroes and J. K. Nørskov, *J. Electroanal. Chem.*, 2007, **607**, 83–89.

46 J. Rossmeisl, A. Logadottir and J. Nørskov, *Chem. Phys.*, 2005, **319**, 178–184.
47 M. J. Craig, G. Coulter, E. Dolan, J. Soriano-López, E. Mates-Torres, W. Schmitt and M. Garca-Melchor, *Nat. Commun.*, 2019, **10**, 4993.
48 T. Shinagawa, A. T. Garcia-Esparza and K. Takanabe, *Sci. Rep.*, 2015, **5**, 13801.
49 I. C. Man, H.-Y. Su, F. Calle-Vallejo, H. A. Hansen, J. I. Martnez, N. G. Inoglu, J. Kitchin, T. F. Jaramillo, J. K. Nørskov and J. Rossmeisl, *ChemCatChem*, 2011, **3**, 1159–1165.
50 N. Govindarajan, J. M. Garca-Lastra, E. J. Meijer and F. Calle-Vallejo, *Curr. Opin. Electrochem.*, 2018, **8**, 110–117.
51 K. S. Exner, *Chem Catal.*, 2021, **1**, 258–271.
52 N. B. Halck, V. Petrykin, P. Krtil and J. Rossmeisl, *Phys. Chem. Chem. Phys.*, 2014, **16**, 13682–13688.
53 M. Busch, N. B. Halck, U. I. Kramm, S. Siahrostami, P. Krtil and J. Rossmeisl, *Nano Energy*, 2016, **29**, 126–135.
54 J. Suntivich, K. J. May, H. A. Gasteiger, J. B. Goodenough and Y. Shao-Horn, *Science*, 2011, **334**, 1383–1385.
55 M. Wohlfahrt-Mehrens and J. Heitbaum, *J. Electroanal. Chem. Interfacial Electrochem.*, 1987, **237**, 251–260.
56 S. Fierro, T. Nagel, H. Baltruschat and C. Comninellis, *Electrochem. Commun.*, 2007, **9**, 1969–1974.
57 J. S. Yoo, X. Rong, Y. Liu and A. M. Kolpak, *ACS Catal.*, 2018, **8**, 4628–4636.
58 A. Grimaud, K. J. May, C. E. Carlton, Y.-L. Lee, M. Risch, W. T. Hong, J. Zhou and Y. Shao-Horn, *Nat. Commun.*, 2013, **4**, 2439.
59 J. T. Mefford, X. Rong, A. M. Abakumov, W. G. Hardin, S. Dai, A. M. Kolpak, K. P. Johnston and K. J. Stevenson, *Nat. Commun.*, 2016, **7**, 11053.
60 X. Rong, J. Parolin and A. M. Kolpak, *ACS Catal.*, 2016, **6**, 1153–1158.
61 A. Grimaud, O. Diaz-Morales, B. Han, W. T. Hong, Y.-L. Lee, L. Giordano, K. A. Stoerzinger, M. T. Koper and Y. Shao-Horn, *Nat. Chem.*, 2017, **9**, 457–465.
62 D. A. Kuznetsov, M. A. Naeem, P. V. Kumar, P. M. Abdala, A. Fedorov and C. R. Müller, *J. Am. Chem. Soc.*, 2020, **142**, 7883–7888.
63 H. Horowitz, J. Longo, H. Horowitz and J. Lewandowski, *ACS Symp. Ser.*, 1985, **279**, 143–163.
64 J. B. Goodenough, R. Manoharan and M. Paranthaman, *J. Am. Chem. Soc.*, 1990, **112**, 2076–2082.
65 M. Ten Kortenaar, J. Vente, D. Ijdo, S. Müller and R. Kötz, *J. Power Sources*, 1995, **56**, 51–60.
66 K. Sardar, S. C. Ball, J. D. Sharman, D. Thompsett, J. M. Fisher, R. A. Smith, P. K. Biswas, M. R. Lees, R. J. Kashtiban and J. Sloan, *et al.*, *Chem. Mater.*, 2012, **24**, 4192–4200.
67 Q. Feng, Q. Wang, Z. Zhang, Y. Xiong, H. Li, Y. Yao, X.-Z. Yuan, M. C. Williams, M. Gu and H. Chen, *et al.*, *Appl. Catal., B*, 2019, **244**, 494–501.
68 Q. Feng, J. Zou, Y. Wang, Z. Zhao, M. C. Williams, H. Li and H. Wang, *ACS Appl. Mater. Interfaces*, 2020, **12**, 4520–4530.
69 D. L. Burnett, E. Petrucco, R. J. Kashtiban, S. F. Parker, J. D. Sharman and R. I. Walton, *J. Mater. Chem. A*, 2021, **9**, 25114–25127.
70 J. Prakash, D. Tryk and E. Yeager, *J. Power Sources*, 1990, **29**, 413–422.
71 J. Prakash, D. Tryk, W. Aldred and E. Yeager, *J. Appl. Electrochem.*, 1999, **29**, 1463–1469.
72 J. Parrondo, M. George, C. Capuano, K. E. Ayers and V. Ramani, *J. Mater. Chem. A*, 2015, **3**, 10819–10828.
73 W. Sun, J.-Y. Liu, X.-Q. Gong, W.-Q. Zaman, L.-M. Cao and J. Yang, *Sci. Rep.*, 2016, **6**, 38429.
74 J. Park, M. Risch, G. Nam, M. Park, T. J. Shin, S. Park, M. G. Kim, Y. Shao-Horn and J. Cho, *Energy Environ. Sci.*, 2017, **10**, 129–136.
75 D. F. Abbott, R. K. Pittkowski, K. Macounova, R. Nebel, E. Marelli, E. Fabbri, I. E. Castelli, P. Krtil and T. J. Schmidt, *ACS Appl. Mater. Interfaces*, 2019, **11**, 37748–37760.
76 G. Zhou, P. Wang, B. Hu, X. Shen, C. Liu, W. Tao, P. Huang and L. Liu, *Nat. Commun.*, 2022, **13**, 4106.
77 J. Park, M. Park, G. Nam, M. G. Kim and J. Cho, *Nano Lett.*, 2017, **17**, 3974–3981.
78 T. Liu, S. Yang, J. Guan, J. Niu, Z. Zhang and F. Wang, *Small Methods*, 2022, **6**, 2101156.
79 P. Wang, Q. Cheng, C. Mao, W. Su, L. Yang, G. Wang, L. Zou, Y. Shi, C. Yan and Z. Zou, *et al.*, *J. Power Sources*, 2021, **502**, 229903.
80 M. Kim, H. Ju and J. Kim, *Dalton Trans.*, 2018, **47**, 15217–15225.
81 C. Iwakura, T. Edamoto and H. Tamura, *Bull. Chem. Soc. Jpn.*, 1986, **59**, 145–148.
82 J. Van Veen, J. Van Der Eijk, R. De Ruiter and S. Huizinga, *Electrochim. Acta*, 1988, **33**, 51–57.
83 A. Kahoul, P. Nkeng, A. Hammouche, F. Naamoune and G. Poillerat, *J. Solid State Chem.*, 2001, **161**, 379–384.
84 G. Gökağaç and B. J. Kennedy, *J. Electroanal. Chem.*, 1994, **368**, 235–239.
85 E.-O. Chi, Y.-U. Kwon and S. Mho, *Bull. Korean Chem. Soc.*, 1997, **18**, 972–975.
86 J. Prakash, D. A. Tryk and E. B. Yeager, *J. Electrochem. Soc.*, 1999, **146**, 4145.
87 K. Sardar, E. Petrucco, C. I. Hiley, J. D. Sharman, P. P. Wells, A. E. Russell, R. J. Kashtiban, J. Sloan and R. I. Walton, *Angew. Chem.*, 2014, **126**, 11140–11144.
88 T. Kinumoto, M. Eto, K. Ono, M. Matsuoka, T. Tsumura and M. Toyoda, *ECS Trans.*, 2017, **75**, 35.
89 D. Lebedev, M. Povia, K. Waltar, P. M. Abdala, I. E. Castelli, E. Fabbri, M. V. Blanco, A. Fedorov, C. Copéret and N. Marzari, *et al.*, *Chem. Mater.*, 2017, **29**, 5182–5191.
90 P.-C. Shih, J. Kim, C.-J. Sun and H. Yang, *ACS Appl. Energy Mater.*, 2018, **1**, 3992–3998.
91 J. Kim, P.-C. Shih, Y. Qin, Z. Al-Bardan, C.-J. Sun and H. Yang, *Angew. Chem.*, 2018, **130**, 14073–14077.
92 C. Shang, C. Cao, D. Yu, Y. Yan, Y. Lin, H. Li, T. Zheng, X. Yan, W. Yu and S. Zhou, *et al.*, *Adv. Mater.*, 2019, **31**, 1805104.
93 M. Kim, H. Ju and J. Kim, *Appl. Catal., B*, 2019, **245**, 29–39.
94 M. Kim, B. Lee, H. Ju, S. W. Lee and J. Kim, *Adv. Mater.*, 2019, **31**, 1901977.

95 P. Gayen, S. Saha and V. Ramani, *ACS Appl. Energy Mater.*, 2020, **3**, 3978–3983.
96 P. Gayen, S. Saha, K. Bhattacharyya and V. K. Ramani, *ACS Catal.*, 2020, **10**, 7734–7746.
97 Q. Feng, Z. Zhao, X.-Z. Yuan, H. Li and H. Wang, *Appl. Catal., B*, 2020, **260**, 118176.
98 P.-C. Shih, C. Zhang, H. Raheja, C.-J. Sun and H. Yang, *ChemNanoMat*, 2020, **6**, 930–936.
99 M. A. Hubert, A. M. Patel, A. Gallo, Y. Liu, E. Valle, M. Ben-Naim, J. Sanchez, D. Sokaras, R. Sinclair and J. K. Nørskov, *et al.*, *ACS Catal.*, 2020, **10**, 12182–12196.
100 V. Celorrio, D. Tiwari, L. Calvillo, A. Leach, H. Huang, G. Granozzi, J. Alonso, A. Aguadero, R. Pinacca and A. Russell, *et al.*, *ACS Appl. Energy Mater.*, 2021, **4**, 176–185.
101 R. K. Pittkowski, D. F. Abbott, R. Nebel, S. Divanis, E. Fabbri, I. E. Castelli, T. J. Schmidt, J. Rossmeisl and P. Krtil, *Electrochim. Acta*, 2021, **366**, 137327.
102 H. Liu, Z. Wang, M. Li, X. Zhao, X. Duan, S. Wang, G. Tan, Y. Kuang and X. Sun, *Sci. China Mater.*, 2021, **64**, 1653–1661.
103 T. Han, J. Wu, X. Lu, Y. Wang, H. Zhao and X. Tang, *J. Solid State Chem.*, 2021, **303**, 122457.
104 C.-L. Ma, Z.-Q. Wang, W. Sun, L.-M. Cao, X.-Q. Gong and J. Yang, *ACS Appl. Mater. Interfaces*, 2021, **13**, 29654–29663.
105 J. Park, H. Jang, S. Y. Lee, J. S. Jeon and M. G. Kim, *J. Mater. Chem. A*, 2022, **10**, 561–569.
106 M. A. Hubert, A. Gallo, Y. Liu, E. Valle, J. Sanchez, D. Sokaras, R. Sinclair, L. A. King and T. F. Jaramillo, *J. Phys. Chem. C*, 2022, **126**, 1751–1760.
107 L. Zhu, C. Ma, Z. Wang, X. Gong, L. Cao and J. Yang, *Appl. Surf. Sci.*, 2022, **576**, 151840.
108 J. Yan, J. Zhu, D. Chen, S. Liu, X. Zhang, S. Yu, Z. Zeng, L. Jiang and F. Du, *J. Mater. Chem. A*, 2022, **10**, 9419–9426.
109 C. Zhang, F. Wang, B. Xiong and H. Yang, *Nano Convergence*, 2022, **9**, 22.
110 H. Liu, Z. Zhang, M. Li, Z. Wang, X. Zhang, T. Li, Y. Li, S. Tian, Y. Kuang and X. Sun, *Small*, 2022, **18**, 2202513.
111 P.-Y. Olu, E. Yokomizo and T. Kinumoto, *ACS Appl. Energy Mater.*, 2022, **5**, 11450–11461.
112 A. Matsumoto, Z.-X. Cai and T. Fujita, *Materials*, 2022, **15**, 6107.
113 S. Sun, Y. Xue, D. Yang, Z. Pei, L. Fang, Y. Xia, R. Ti, C. Wang, C. Liu and B. Xiong, *et al.*, *Chem. Eng. J.*, 2022, **448**, 137580.
114 X. Ping, Y. Liu, S. Chen, N. Ran, L. Zheng, M. Wang, L. Guo and Z. Wei, *Appl. Catal., B*, 2022, **318**, 121884.
115 N. Zhang, C. Wang, J. Chen and Y. Chai, *EcoMat*, 2023, **5**, e12290.
116 N. Han, S. Feng, Y. Liang, J. Wang, W. Zhang, X. Guo, Q. Ma, Q. Liu, W. Guo and Z. Zhou, *et al.*, *Adv. Funct. Mater.*, 2023, 2208399.
117 D. Galyamin, J. Torrero, I. Rodrguez, M. J. Kolb, P. Ferrer, L. Pascual, M. A. Salam, D. Gianolio, V. Celorrio and M. Mokhtar, *et al.*, *Nat. Commun.*, 2023, **14**, 2010.
118 Y. Wang, H. Zhao, Y. Guo, J. Wu, X. Lu and X. Tang, *Nanoscale*, 2023, **15**, 9413–9422.
119 G. Lee, Y. Cho, E. Jang and J. Kim, *Appl. Surf. Sci.*, 2023, **627**, 157301.
120 J. Zhang, L. Shi, R. Tong and L. Yang, *ACS Appl. Mater. Interfaces*, 2023, **15**, 52358–52367.
121 B. Yin, C. Liu, X. Li, X. Dong, D. Chen, Q. Li, D. Chen and Z. Wang, *Mater. Lett.*, 2023, **351**, 134987.
122 Q. Zhang, T. Liu, H. Guo, Y. Chen, Y. Di, Z. Zhang and F. Wang, *Adv. Funct. Mater.*, 2023, 2306176.
123 F. Shang, B. Wang, B. An, H. He, Y. Shui, H. Cai, C. Liang and S. Yang, *Small*, 2023, 2310323.
124 S. Chandrasekaran, E. Arumugam, S. Ramasamy, C. Karuppiah, S. Bhaskaran, C.-C. Yang, D. Nallapandi and K. Palanisamy, *Int. J. Hydrogen Energy*, 2023, **48**, 10423–10437.
125 G. Lee, W. Yang and J. Kim, *J. Alloys Compd.*, 2024, **970**, 172484.
126 H. Guo, Z. Zhang and F. Wang, *J. Materiomics*, 2024, **10**, 1234–1242.
127 J. Zhang, L. Shi, X. Miao, S. Zhou and L. Yang, *ACS Appl. Mater. Interfaces*, 2024, **16**, 21905–21914.
128 R. Yang, Q. Hao, J. Zhao, C. Lei, S. Xue, F. Miao, W. Tang, Q. Huang, J. Wang and Y. Wu, *J. Alloys Compd.*, 2024, **986**, 174072.
129 G. Lee, E. Jang, P. Su and J. Kim, *Appl. Surf. Sci.*, 2024, 159788.
130 R. D. Shannon, *Found. Crystallogr.*, 1976, **32**, 751–767.
131 T. Zhang, A. Coughlin, C.-K. Lu, J. Heremans and S. Zhang, *J. Phys.: Condens. Matter*, 2024, **36**, 273001.
132 C. Petit, J. Rehspringer, A. Kaddouri, S. Libs, P. Poix and A. Kiennemann, *Catal. Today*, 1992, **13**, 409–416.
133 D. R. Lide, *CRC handbook of chemistry and physics: a ready-reference book of chemical and physical data*, CRC Press, 1995.
134 P. M. Woodward, P. Karen, J. S. Evans and T. Vogt, *Solid state materials chemistry*, Cambridge University Press, 2021.
135 K. Fujii, Y. Sato, S. Takase and Y. Shimizu, *J. Electrochem. Soc.*, 2014, **162**, F129.
136 H. Lee, O. Gwon, K. Choi, L. Zhang, J. Zhou, J. Park, J.-W. Yoo, J.-Q. Wang, J. H. Lee and G. Kim, *ACS Catal.*, 2020, **10**, 4664–4670.
137 M. Mavrikakis, B. Hammer and J. K. Nørskov, *Phys. Rev. Lett.*, 1998, **81**, 2819.
138 M. Heath, H. Erring, K. Mathisen, S. Sunde and F. Seland, *Electrochim. Acta*, 2025, 146476.
139 G. Berti, S. Sanna, C. Castellano, J. Van Duijn, R. Ruiz-Bustos, L. Bordonali, G. Bussetti, A. Calloni, F. Demartin and L. Duo, *et al.*, *J. Phys. Chem. C*, 2016, **120**, 11763–11768.
140 J. Zhang, X. Fu, F. Xia, W. Zhang, D. Ma, Y. Zhou, H. Peng, J. Wu, X. Gong and D. Wang, *et al.*, *Small*, 2022, **18**, 2108031.
141 J. He, X. Zhou, P. Xu and J. Sun, *Adv. Energy Mater.*, 2021, **11**, 2102883.
142 D. Escalera-López, S. Czioska, J. Geppert, A. Boubnov, P. Rose, E. Saraci, U. Krewer, J.-D. Grunwaldt and S. Cherevko, *ACS Catal.*, 2021, **11**, 9300–9316.

143 A. H. Reksten, H. Thuv, F. Seland and S. Sunde, *J. Electroanal. Chem.*, 2018, **819**, 547–561.
144 S. B. Scott, R. R. Rao, C. Moon, J. E. Sørensen, J. Kibsgaard, Y. Shao-Horn and I. Chorkendorff, *Energy Environ. Sci.*, 2022, **15**, 1977–1987.
145 L.-E. Owe, M. Tsypkin and S. Sunde, *Electrochim. Acta*, 2011, **58**, 231–237.
146 A. T. Marshall and L. Vaisson-Béthune, *Electrochem. Commun.*, 2015, **61**, 23–26.
147 A. T. Marshall, *Curr. Opin. Electrochem.*, 2018, **7**, 75–80.
148 S. Watzele and A. S. Bandarenka, *Electroanalysis*, 2016, **28**, 2394–2399.
149 D. A. Harrington and B. E. Conway, *Electrochim. Acta*, 1987, **32**, 1703–1712.
150 S. Ardizzone, G. Fregonara and S. Trasatti, *Electrochim. Acta*, 1990, **35**, 263–267.
151 T. Binninger, R. Mohamed, K. Waltar, E. Fabbri, P. Levecque, R. Kötz and T. J. Schmidt, *Sci. Rep.*, 2015, **5**, 12167.
152 C. Spöri, J. T. H. Kwan, A. Bonakdarpour, D. P. Wilkinson and P. Strasser, *Angew. Chem., Int. Ed.*, 2017, **56**, 5994–6021.
153 F.-Y. Chen, Z.-Y. Wu, Z. Adler and H. Wang, *Joule*, 2021, **5**, 1704–1731.
154 F. Zeng, C. Mebrahtu, L. Liao, A. K. Beine and R. Palkovits, *J. Energy Chem.*, 2022, **69**, 301–329.
155 C. Rong, K. Dastafkan, Y. Wang and C. Zhao, *Adv. Mater.*, 2023, **35**, 2211884.
156 Q. Feng, G. Liu, B. Wei, Z. Zhang, H. Li and H. Wang, *et al.*, *J. Power Sources*, 2017, **366**, 33–55.
157 A. Zagalskaya, P. Chaudhary and V. Alexandrov, *J. Phys. Chem. C*, 2023, **127**, 14587–14598.
158 S. Cherevko, A. R. Zeradjanin, A. A. Topalov, N. Kulyk, I. Katsounaros and K. J. Mayrhofer, *ChemCatChem*, 2014, **6**, 2219–2223.
159 K. A. Stoerzinger, O. Diaz-Morales, M. Kolb, R. R. Rao, R. Frydendal, L. Qiao, X. R. Wang, N. B. Halck, J. Rossmeisl and H. A. Hansen, *et al.*, *ACS Energy Lett.*, 2017, **2**, 876–881.
160 S. Hao, M. Liu, J. Pan, X. Liu, X. Tan, N. Xu, Y. He, L. Lei and X. Zhang, *Nat. Commun.*, 2020, **11**, 5368.
161 K. Kadakia, M. K. Datta, O. I. Velikokhatnyi, P. H. Jampani and P. N. Kumta, *Int. J. Hydrogen Energy*, 2014, **39**, 664–674.
162 R. Kötz, H. Lewerenz and S. Stucki, *J. Electrochem. Soc.*, 1983, **130**, 825.
163 S. Geiger, O. Kasian, A. M. Mingers, S. S. Nicley, K. Haenen, K. J. Mayrhofer and S. Cherevko, *ChemSusChem*, 2017, **10**, 4140–4143.
164 H.-S. Oh, H. N. Nong, T. Reier, A. Bergmann, M. Gliech, J. Ferreira de Araújo, E. Willinger, R. Schlogl, D. Teschner and P. Strasser, *J. Am. Chem. Soc.*, 2016, **138**, 12552–12563.
165 C. Daiane Ferreira da Silva, F. Claudel, V. Martin, R. Chattot, S. Abbou, K. Kumar, I. Jiménez-Morales, S. Cavaliere, D. Jones and J. Rozière, *et al.*, *ACS Catal.*, 2021, **11**, 4107–4116.
166 X. Wang, Z.-G. Shao, G. Li, L. Zhang, Y. Zhao, W. Lu and B. Yi, *Int. J. Hydrogen Energy*, 2013, **38**, 9057–9064.
167 S. M. Skaftun, S. Sunde, G. M. Haarberg and F. Seland, *ECS Trans.*, 2018, **85**, 103.
168 S. Geiger, O. Kasian, M. Ledendecker, E. Pizzutilo, A. M. Mingers, W. T. Fu, O. Diaz-Morales, Z. Li, T. Oellers and L. Fruchter, *et al.*, *Nat. Catal.*, 2018, **1**, 508–515.
169 C. Kuai, Z. Xu, C. Xi, A. Hu, Z. Yang, Y. Zhang, C.-J. Sun, L. Li, D. Sokaras and C. Dong, *et al.*, *Nat. Catal.*, 2020, **3**, 743–753.
170 C. C. McCrory, S. Jung, J. C. Peters and T. F. Jaramillo, *J. Am. Chem. Soc.*, 2013, **135**, 16977–16987.
171 L. Giordano, B. Han, M. Risch, W. T. Hong, R. R. Rao, K. A. Stoerzinger and Y. Shao-Horn, *Catal. Today*, 2016, **262**, 2–10.